Mobility of Calcium Channels in the Presynaptic Membrane

Highlights

- Calcium channels (VDCC) are mobile yet confined within the presynaptic membrane

- Intracellular Ca^{2+} chelation by BAPTA or EGTA reduces VDCC mobility

- Increasing VDCC surface expression by $\alpha 2\delta 1$ leaves synaptic VDCC density unaffected

- Simulations suggest mobility-dependent equalization of synaptic release probability

Authors

Romy Schneider, Eric Hosy, ..., Andreas Voigt, Martin Heine

Correspondence

martin.heine@lin-magdeburg.de

In Brief

By single-molecule tracking, Schneider et al. demonstrate the dynamic organization of presynaptic calcium channel populations in hippocampal neurons. The data suggest that channel mobility promotes cooperativity of calcium influx and serves as a potential means to control vesicle release probability.

CrossMark

CellPress

Mobility of Calcium Channels in the Presynaptic Membrane

Romy Schneider,[1] Eric Hosy,[4,5] Johannes Kohl,[7] Julia Klueva,[1,3] Daniel Choquet,[4,5,6] Ulrich Thomas,[2] Andreas Voigt,[8] and Martin Heine[1,*]
[1]Molecular Physiology Group
[2]Department Neurochemistry
[3]Presynaptic Plasticity Group
Leibniz Institute for Neurobiology, D-39118 Magdeburg, Germany
[4]University of Bordeaux
[5]CNRS, Interdisciplinary Institute for Neuroscience, UMR 5297
[6]Bordeaux Imaging Center, UMS 3420 CNRS, US4 INSERM, University of Bordeaux
F-33000 Bordeaux, France
[7]Harvard University, Department Molecular and Cellular Biology, Cambridge, MA 02138, USA
[8]Otto-von-Guericke-University Magdeburg, Systemverfahrenstechnik, Universitätsplatz 2, D-39106 Magdeburg, Germany
*Correspondence: martin.heine@lin-magdeburg.de
http://dx.doi.org/10.1016/j.neuron.2015.03.050

SUMMARY

Unravelling principles underlying neurotransmitter release are key to understand neural signaling. Here, we describe how surface mobility of voltage-dependent calcium channels (VDCCs) modulates release probabilities (P_r) of synaptic vesicles (SVs). Coupling distances of <10 to >100 nm have been reported for SVs and VDCCs in different synapses. Tracking individual VDCCs revealed that within hippocampal synapses, ~60% of VDCCs are mobile while confined to presynaptic membrane compartments. Intracellular Ca^{2+} chelation decreased VDCC mobility. Increasing VDCC surface populations by co-expression of the $\alpha 2\delta 1$ subunit did not alter channel mobility but led to enlarged active zones (AZs) rather than higher channel densities. VDCCs thus scale presynaptic scaffolds to maintain local mobility. We propose that dynamic coupling based on mobile VDCCs supports calcium domain cooperativity and tunes neurotransmitter release by equalizing P_r for docked SVs within AZs.

INTRODUCTION

The molecular architecture of active zones (AZs) ensures the precision and adjustability of synaptic vesicle (SV) release. This involves a tight coupling of presynaptic voltage-dependent calcium channels (VDCCs) and calcium sensor proteins on docked SVs. Experimentally, differential shaping of intracellular calcium domains by chelators such as EGTA and BAPTA has been used to assess channel-sensor coupling and modeling has led to various testable hypotheses (Eggermann et al., 2012). Protein-protein interactions that directly or indirectly link VDCCs to SVs are described (Catterall, 1999; Davydova et al.,

2014; Kaeser et al., 2011; Liu et al., 2011; Wong et al., 2014). However, the precise modalities of channel-sensor coupling, in particular its dynamic aspects, remain unclear. Tight coupling of 10–20 nm was uncovered for cortical GABAergic Schaffer collateral and glutamatergic cerebellar synapses (Bucurenciu et al., 2008; Schmidt et al., 2013). In this scenario, a single channel opening can trigger vesicular fusion and release probabilities (P_r) may be rather uniform as long as channels are evenly distributed within AZs and exceed the number of docked vesicles (Ermolyuk et al., 2013; Holderith et al., 2012; Scimemi and Diamond, 2012). Loose coupling of 100 nm along with higher VDCC numbers were reported for other types of synapses and probably contributes to presynaptic plasticity (Borst and Sakmann, 1996; Meinrenken et al., 2002; Vyleta and Jonas, 2014). P_r even varies considerably between synapses in single axons, i.e., for a given type of synapse. Such fluctuations can result from differences in the number of readily releasable SVs but also from synapse-specific rates of Ca^{2+} influx due to maturation- or plasticity-related differences in the subtype composition, activity state, local density, and positioning of Ca^{2+} channels (Holderith et al., 2012; Ermolyuk et al., 2012; Li et al., 2007; Reid et al., 1997).

Assuming a low to moderate density of VDCCs within AZs, we wondered whether VDCC mobility contributes to a dynamic mode of channel-sensor coupling. Using single particle tracking-photoactivated localization microscopy (sptPALM), we monitored mEOS2-tagged $\alpha 1$ calcium channel subunits at high spatio-temporal resolution in cultured hippocampal neurons. We found that a substantial fraction of $Ca_V 2.1$ (P/Q)- and $Ca_V 2.2$ (N)-type channels is mobile within presynaptic areas. We assessed various parameters for their impact on channel mobility and found that it is largely unaffected by $\alpha 2\delta 1$ subunit-mediated increase in synaptic VDCC abundance and by an acute depletion of the readily releasable pool (RRP) of SVs. In contrast, intracellular calcium chelation uncovered Ca^{2+}-dependent regulation of channel mobility. To integrate these findings, we performed computational modeling, which suggests that the interplay between channel densities, mobility, and Ca^{2+} influx

determines calcium domain cooperativity between adjacent channels and thus serves as a potential means to control P_r.

RESULTS

Expression of Tagged VDCCs Preserves Normal Synaptic Phenotypes

The surface dynamics of presynaptic VDCCs has been addressed by tracking the $\alpha 2\delta 4$ subunit (Mercer et al., 2011) or extracellularly tagged $\alpha 1$ subunits (Di Biase et al., 2011). These insightful studies were limited by promiscuous associations of $\alpha 2\delta$ subunits with $\alpha 1$ subunits (Hoppa et al., 2012), compromised channel function, or reduced accessibility for fluorophores under physiological conditions. To overcome these obstacles, we used sptPALM (Manley et al., 2008). We fused the photoconvertible fluorophore mEOS2 or GFP to the cytoplasmic N termini of $Ca_V2.1$ and $Ca_V2.2$ $\alpha 1$ subunits and validated channel function in HEK cells (Figures S1A–S1F). Next, we assessed synaptic targeting of tagged $\alpha 1$ subunits in hippocampal neurons by co-staining for Rab3 interacting molecule (RIM 1/2) and Bassoon, two prominent components of the cytomatrix at the AZ (CAZ) involved in presynaptic localization of VDCCs (Davydova et al., 2014; Kaeser et al., 2011). Tagged VDCCs co-localized with both RIM and Bassoon, similar to endogenous channels in non-transfected cells (Figures S1G–S1I).

Patch-clamp recordings from synaptically coupled hippocampal neurons in the presence of isoform-specific channel blockers revealed that the relative contribution of $Ca_V2.1$ and $Ca_V2.2$ to transmission remained unaffected when tagged $Ca_V2.1$ was expressed, whereas expression of $Ca_V2.2$ resulted in $Ca_V2.2$-dominated synapses (Figure S1J). Using an antibody specific for rodent but not human $Ca_V2.1$ (Figures S2A and S2B), we found that endogenous $Ca_V2.1$ was completely replaced by $Ca_V2.1$::GFP at about 60% of synapses and partially replaced at remaining synapses (Figures S2C and S2D). Consistent with previous reports (Cao and Tsien, 2010; Hoppa et al., 2012), expression of $Ca_V2.2$::GFP virtually abolished the contribution of $Ca_V2.1$ to synaptic transmission (Figure S1J). Paired-pulse ratios (PPRs) from synaptically connected neurons remained unaffected by expression of either $Ca_V2.1$::GFP or $Ca_V2.2$::GFP (Figure S1K). Expression of tagged $Ca_V2.1$ thus allows monitoring of its presynaptic distribution under conditions close to the mature state of natural synapses whereas the predominance of $Ca_V2.2$ upon expression of tagged $Ca_V2.2$ mimics channel composition of synapses in young hippocampal neurons (Scholz and Miller, 1995).

Calcium Channels Display Confined Mobility within Presynaptic Membranes

To assess the mobility of individual channels, we applied sptPALM on cells expressing mEOS2-tagged $\alpha 1$ subunits. Experiments on fixed COS7 cells revealed a localization accuracy of 21.4 ± 4 nm for a 30 ms integration time per frame, and similar accuracy (27.7 ± 10 nm) was obtained for immobile molecules in living neurons (Figures S2E–S2G). Spontaneous uptake of fluorescently labeled antibodies against synaptotagmin-1 (Syt1) uncovered active synapses (see Supplemental Information).

Epifluorescence and sptPALM revealed that prominent clusters of $Ca_V2.1$::mEOS2 or $Ca_V2.2$::mEOS2 were mostly associated with Syt1-positive boutons, whereas extrasynaptic channel distribution appeared largely diffuse (Figures 1A and 1B). SptPALM also revealed that outside clusters most channels are mobile. Inside synaptic clusters both immobile and mobile molecules were found (Figures 1A and 1B). Plotting the mean square displacement (MSD) over time intervals clearly indicated that the majority of $Ca_V2.1$::mEOS2 and $Ca_V2.2$::mEOS2 molecules are freely mobile outside synapses and either mobile (yet spatially confined) or immobile within synapses (Figures 1C and 1D). Comparing diffusion coefficients from synaptic and extrasynaptic channel populations revealed clear differences (Figures 1F and 1G). Within synapses, 35%–45% of the channels are immobile (median diffusion coefficient < 0.002 μm^2/s), whereas elsewhere along axons only about 20% of channels are immobile. While all remaining channel molecules are mobile, they move faster outside synapses (Figures 1F and 1G). Notably, synaptic $Ca_V2.1$::mEOS2 and $Ca_V2.2$::mEOS2 displayed similar mobility (median diff.–coeff. $Ca_V2.1$-mEOS2 0.01 μm^2/s interquartile range [IQR] 0.005–0.03 μm^2/s, median diff.–coeff. $Ca_V2.2$-mEOS2 0.014 μm^2/s IQR 0.006–0.04 μm^2/s; Figures 1F, 1G, and 2C). The short lifetime of mEOS2 fluorescence precluded direct assessments of dwell times for synaptic channel populations. However, single molecules exchanging between synaptic and extrasynaptic membrane compartments could be observed (Figures 1A and 1B). To test whether the mobility profiles are characteristic for VDCCs or a general feature of presynaptic membrane proteins, we monitored tagged syntaxin-1A, a presynaptic *t*-SNARE. Syntaxin-1A::mEOS2 displayed high mobility and, in contrast to VDCCs, no confinement within synapses (Figures 1E and 1H). Consistent with previous findings (Ribault et al., 2011), the synaptic exchange rate for syntaxin-1A molecules appeared high and a fraction of ~15% immobile syntaxin-1A::mEOS2 molecules could reflect temporal immobilization of syntaxin-1A in synapses. These experiments demonstrate that despite the need for tight channel-sensor coupling, a large population of channels (~60%) is dynamic but confined within presynaptic membranes. This observation was corroborated by calculating the radius of confinement as a measure of the mean surface area explored by channel molecules in the presynaptic compartment ($Ca_V2.1$::mEOS2, median r_{conf} 107.2 nm, IQR 73.32/157.5 nm; $Ca_V2.2$::mEOS2, median r_{conf} 133.7 nm, IQR 93.4/211.4 nm; Figure 2E). These measures clearly exceeded coupling distances deduced from electrophysiological data (Borst and Sakmann, 1996; Bucurenciu et al., 2008; Meinrenken et al., 2002; Schmidt et al., 2013; Scimemi and Diamond, 2012; Vyleta and Jonas, 2014).

Channel Mobility Is Unaffected by Channel Numbers within the Presynaptic Membrane

We reasoned that as a determinant for SV release, the mobility of synaptic VDCCs might be influenced by local channel density, RRP size, Ca^{2+} influx, and Ca^{2+} buffering. To manipulate these parameters, we first co-expressed tagged $Ca_V2.1$ or $Ca_V2.2$ with the $\alpha 2\delta 1$ subunit to increase presynaptic channel density and P_r (Hoppa et al., 2012). Indeed, anti-GFP fluorescence intensities (Figures S3A–S3E) and the counting of synapse-confined
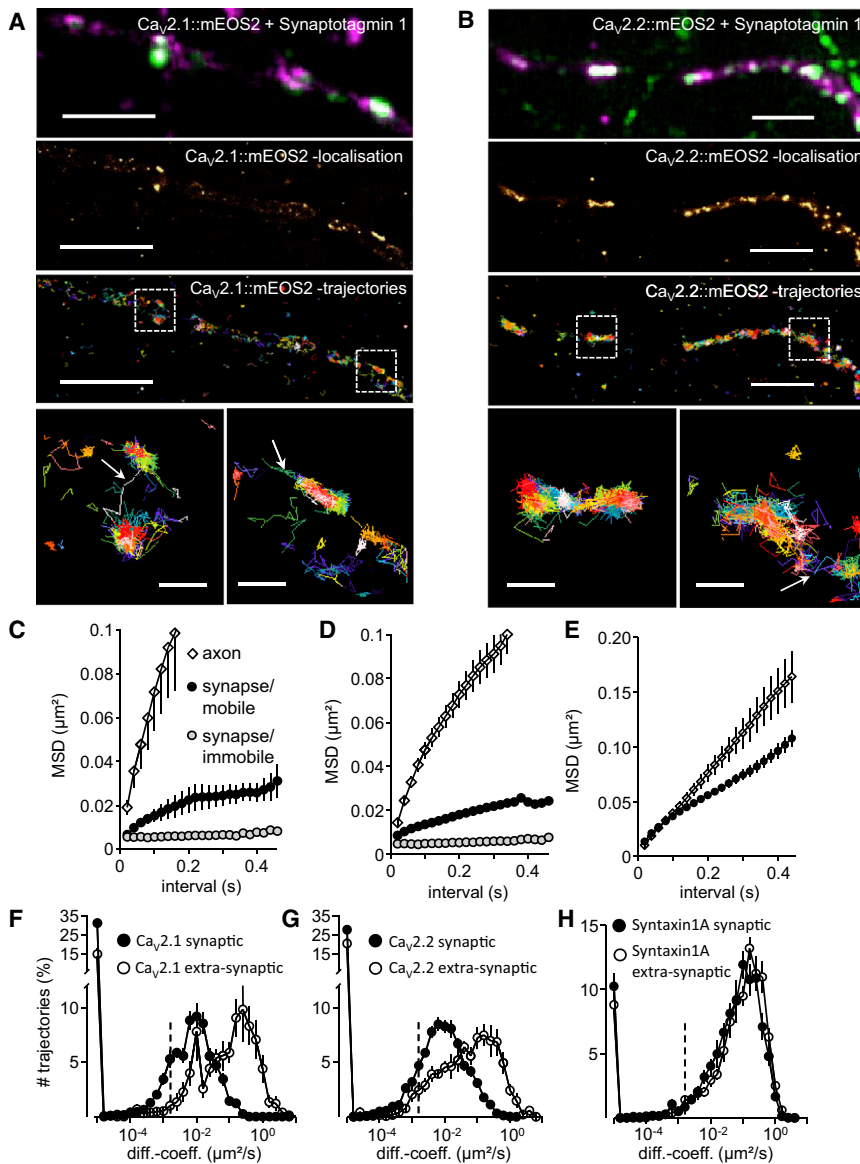
Figure 1. Synaptic and Extrasynaptic Mobility of VDCCs and Syntaxin1A

(A and B) $Ca_V2.1$::mEOS2 and $Ca_V2.2$::mEOS2 (green) enrich at hippocampal synapses revealed by uptake of anti-Syt1 (magenta). Second row displays localization of channel molecules within a focal plane. Third row shows trajectories of channel molecules along axonal segments with selected regions enlarged below. Few channels escaping synaptic areas indicate exchange between compartments (arrows). Scale bars: 3 μm, 0.5 μm for zoomed examples. (C–E) Plot of mean square displacement (MSD) over time intervals for axonal, synaptic mobile, and immobile $Ca_V2.1$::mEOS2 (C; n = 32/105/60 for axonal/synaptic mobile/synaptic immobile trajectories), $Ca_V2.2$::mEOS2 (D; 425/420/227), and Syntaxin1A::mEOS2 (E; n = 538/130 for axonal/synaptic mobile trajectories). (F–H) Normalized distribution of diffusion coefficients for $Ca_V2.1$::mEOS2 (F; n = 612/3281 for axonal/synaptic trajectories), $Ca_V2.2$::mEOS2 (G; 5046/22681), and Syntaxin1A (H; 5849/30139). Dotted lines mark threshold for immobile fractions (D < 0.002 μm²/s). Data in (C)–(H) are from 2–5 neuronal cultures 14–21 DIV.

aptic Bassoon or RIM levels, whereas $Ca_V2.2$::GFP alone exerted a strong effect. Co-expression with α2δ1 further increased synaptic Bassoon and RIM fluorescence for each of the tagged channel isoforms, reaching maximum levels when $Ca_V2.2$::GFP and α2δ1 were co-expressed (Figures S3F and S3G). Elevated Bassoon or RIM immunofluorescence could reflect higher synaptic protein density or enlarged CAZs. We therefore used stimulated emission depletion (STED) microscopy to determine the spatial extension of Bassoon and RIM clusters by 2D Gauss fittings (Figures 3A and 3B). This revealed that Bassoon and RIM clusters

trajectories as a relative measure for channel numbers (Figures 2A and 2B) revealed that α2δ1 co-expression led to a substantial increase in the number of synaptic VDCCs and to markedly increased synaptic activity (Figure S3G).

Modeling channel dynamics within a confined area predicts that an increase in channel density reduces channel mobility (see below; Figures S4A and S4C). However, co-expression of α2δ1 did not alter channel mobility for $Ca_V2.1$::mEOS2 and only slightly decreased it for $Ca_V2.2$::mEOS2 (Figures 2C and 2D). The radius of confinement did not change for $Ca_V2.1$ and decreased only moderately for $Ca_V2.2$ (Figure 2E). This suggested that synaptic channel densities had remained largely unaffected. Inspection of Bassoon- and RIM-specific immunofluorescence rather pointed to a concomitant enlargement of the CAZ. Quantitative analysis showed that overexpression of α2δ1 alone increased synaptic Bassoon and RIM levels (Figures S3F and S3G). Expression of $Ca_V2.1$::GFP did not increase syn-

indeed became enlarged due to expression of $Ca_V2.1$::GFP, $Ca_V2.2$::GFP, and/or α2δ1 (Figures 3A–3C). We propose that the CAZ and its scaffold proteins define an area of confinement for synaptic calcium channels which scales with channel number in a manner that leaves synaptic channel density and mobility largely constant.

Synaptic VDCC Mobility Is Regulated by Free Intracellular Calcium

To assess effects of presynaptic Ca^{2+} on channel mobility, we used two different calcium chelators, BAPTA-AM and EGTA-AM. Altering cytosolic calcium buffer capacities by exogenously applied chelators strongly influences P_r (Awatramani et al., 2005; Ermolyuk et al., 2013; Williams et al., 2012). We monitored changes in P_r in neurons preloaded with BAPTA-AM or EGTA-AM by measuring mEPSCs. Both chelators strongly increased the interevent interval but did not alter mEPSC amplitudes
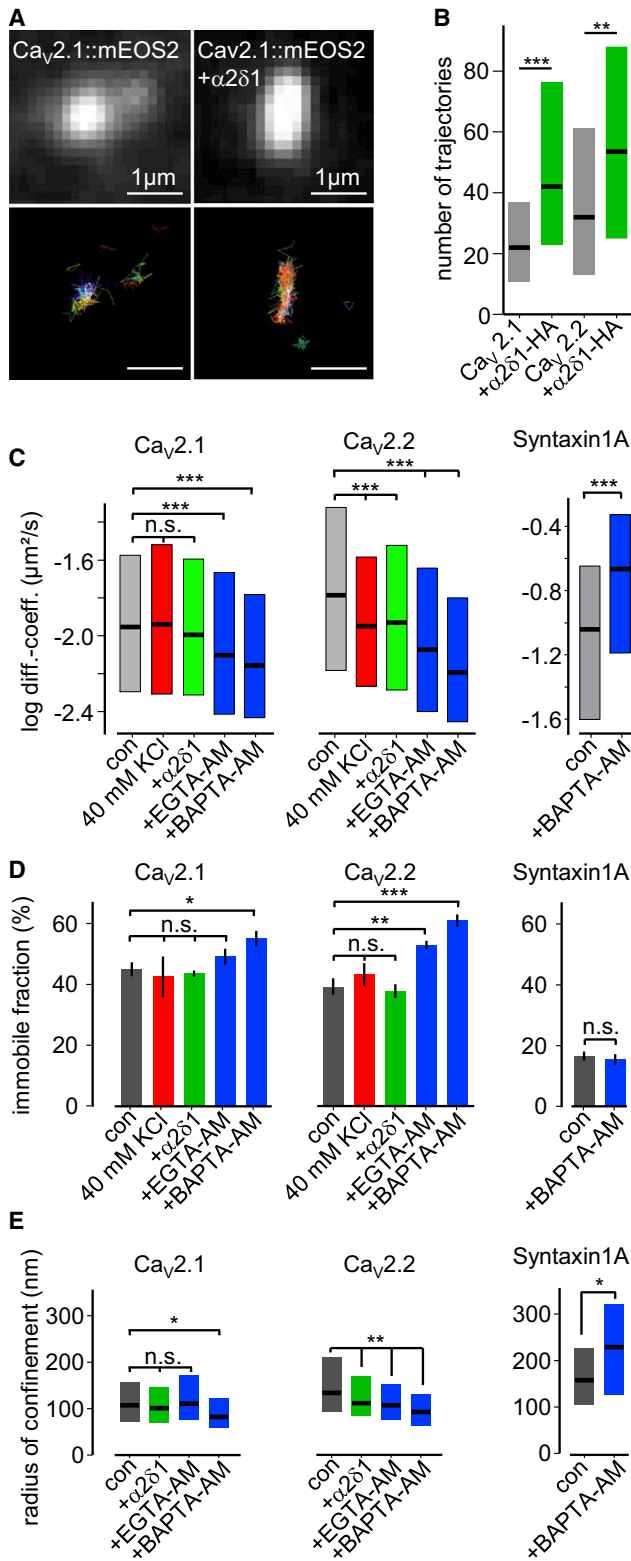
Figure 2. Calcium Channel Surface Expression and Mobility under Varying Conditions

(A and B) Effect of α2δ1 expression on Ca$_V$::mEOS2 surface expression, exemplified for synaptic Ca$_V$2.1 in (A) and quantified for both channel subtypes

(Figures S4E–S4H). At the same time, both chelators decreased the mobility of Ca$_V$2.1::mEOS2 and Ca$_V$2.2::mEOS2 and increased the fraction of immobile channels. EGTA-AM primarily affected Ca$_V$2.2::mEOS2 mobility, whereas BAPTA-AM affected both channel isoforms, increasing the rate of immobile synaptic channels to 55%–60% (Figures 2C and 2D). The radius of confinement dropped below 100 nm (Ca$_V$2.1::mEOS2, median r$_{conf}$ 82.1 nm, IQR 57.7/121.8 nm; Ca$_V$2.2::mEOS2, median r$_{conf}$ 92.5 nm, IQR 62.4/130.8 nm; Figure 2E). In contrast, the mobility and radius of confinement of syntaxin-1A increased, whereas its immobile fraction remained unaltered (Figures 2C–2E).

Considering the negative effect of Ca^{2+} chelation on synaptic channel mobility, we wondered whether increased Ca^{2+} influx would act oppositely. KCl-triggered depolarization increased mEPSC frequency during the first minutes (Figures S4E–S4H) but left overall synaptic mobility of Ca$_V$2.1 unaltered and modestly decreased Ca$_V$2.2 mobility (Figures 2C and 2D). This implies that a boost of fusion events leading to the depletion of the RRP has little effect on the mobility of VDCCs. We thus conclude that acute global changes in [Ca^{2+}]$_i$ within the physiological range do not significantly affect the dynamics of VDCCs. In contrast, altered Ca^{2+} buffering capacity reduces spontaneous activity, impacts on the shape of the Ca^{2+} domain upon channel opening, and may also change the dynamics and relative positioning of synaptic molecules such as VDCCs and syntaxin-1A, either by Ca^{2+} buffering or reduced activity and hence lower membrane turnover.

Modeling the Contribution of VDCC Mobility to Synaptic Transmission

Our observations suggest that the local stochastic mobility of VDCCs is tightly controlled within the synapse and might contribute to activity-related Ca^{2+} fluctuations. To illustrate this hypothesis, we used Monte Carlo simulations to model the Ca^{2+} signal while considering the stochastic motion of VDCCs and setting the open probability for the channel population to 0.5 within synapses. Vesicular release depends on local changes of [Ca^{2+}]$_i$ within less than 100 nm around SVs (Eggermann et al., 2012) and at a depth of 5–10 nm. We thus wondered whether the observed stability of local channel density relates to [Ca^{2+}]$_i$ fluctuations. Comparing [Ca^{2+}]$_i$ fluctuations of small, intermediate, or large channel populations within the same area of

in (B). Scale bar: 1 μm. (B) Synaptic Ca$_V$2::mEOS2 trajectories > 8 points (2 cultures, Ca$_V$2.1::mEOS2 n = 97 synapses, +α2δ1, n = 77; Ca$_V$2.2::mEOS2 n = 51, +α2δ1, n = 50). (C) Diffusion coefficient of mobile fractions (D > 0.002 μm²/s) of Ca$_V$2.1::mEOS2, Ca$_V$2.2::mEOS2, and Syntaxin1A::mEOS2 under conditions as indicated (Ca$_V$2.1::mEOS2: n$_{con}$ = 1,794/ n$_{KCl}$ = 1,280/ n$_{α2δ1}$ = 7,681/ n$_{EGTA}$ = 5,275/ n$_{BAPTA}$ = 1,457; Ca$_V$2.2::mEOS2: n$_{con}$ = 1,734/ n$_{KCl}$ = 2,518/ n$_{α2δ1}$ = 11,087/ n$_{EGTA}$ = 8,870/ n$_{BAPTA}$ = 2,487; Syntaxin1A::mEOS2: n$_{con}$ = 21,289/ n$_{BAPTA}$ = 26,661, data from 2–5 cultures, probed by Kruskal-Wallis test followed by Dunn's test). (D) Immobile fractions of Ca$_V$2.1::mEOS2, Ca$_V$2.2::mEOS2, and Syntaxin1A::mEOS2 under various conditions. (E) Radius of confinement of mobile channels and syntaxin1A within synapses given as medians and interquartile range. Data from 2–5 cultures, probed by one-way ANOVA test followed by Dunnett's test (Ca$_V$2.1::mEOS2: n = 153 synapses, +α2δ1 n = 278, +EGTA-AM n = 293, +BAPTA-AM n = 97; Ca$_V$2.2::mEOS2: n = 512, +α2δ1 n = 247, +EGTA-AM n = 96, +BAPTA-AM n = 40; syntaxin1A: n = 105).
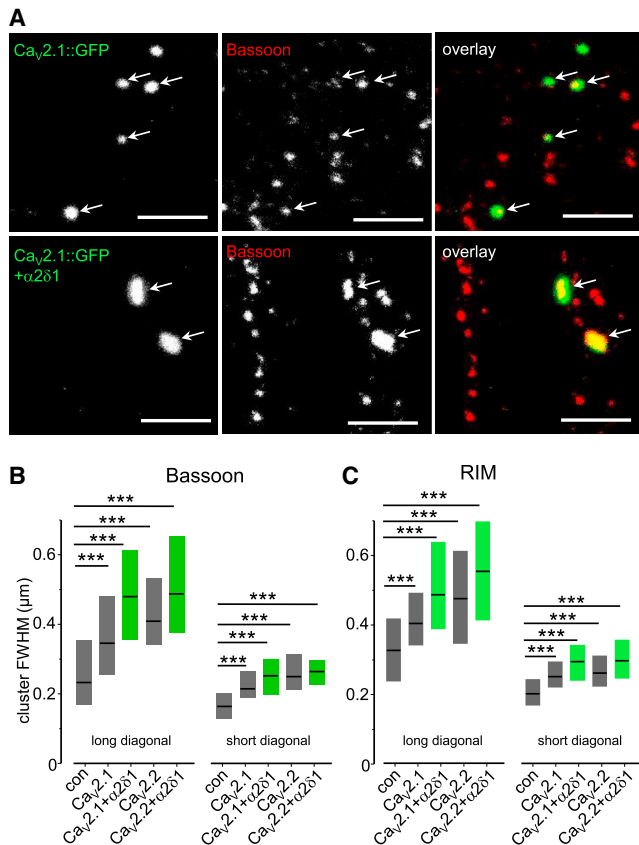
Figure 3. Enlarged AZ upon Co-Expression of α1 and α2δ1 Subunits
(A) $Ca_V2.1$::GFP (confocal) and Bassoon-clusters (STED) in neurons co-transfected with $Ca_V2.1$::GFP and α2δ1 are bigger (arrows) than in $Ca_V2.1$::GFP only or non-transfected neurons. Scale bars: 2 μm. (B and C) Lengths (principal) and widths (auxiliary) of Bassoon and RIM protein domains determined by 2D Gauss fitting. Data are shown as median with interquartile range from 2 cultures tested by Kruskal-Wallis test followed by a Dunn's test (Bassoon clusters: n_{con} = 1,197 synapses, $n_{CaV2.1::GFP}$ = 92, $n_{+α2δ1}$ = 96; $n_{CaV2.2::GFP}$ = 64, $n_{+α2δ1}$ = 95; RIM clusters: n_{con} = 237 synapses, $n_{CaV2.1::GFP}$ = 184, $n_{+α2δ1}$ = 176; $n_{CaV2.2::GFP}$ = 99, $n_{+α2δ1}$ = 153).

confinement accompanied by a reduction in channel mobility uncovered large differences in the coefficient of variation (CV) for local presynaptic Ca^{2+} transients (Figure 4A). The amplitude of total calcium increases with channel numbers. The CV, however, peaked for intermediate channel densities where channel mobility is close to the one determined experimentally (Figure 4B). Increasing channel density induces a decrease in channel mobility due to molecular crowding effects (Figure S4C). The model implies that channel density and channel dynamics are adjusted close to maximal CV of local Ca^{2+} transients within the presynaptic compartment. This correlation holds true for different membrane surfaces without changes in channel density (Figure 4B). Estimating synaptic channel density by taking the median size of Bassoon clusters as average surface area of AZs and measured numbers of trajectories as a measure for channel numbers yielded ~175 channels per μm². Considering that this estimation is biased by the blinking of mEOS2 (Figure S2E) and persistent endogenous VDCCs (Figures S2C and

S2D), channel densities for the maximal CV in our model get close to those determined experimentally (Figure 4B, inset). It is conceivable that channel density is optimized to ensure local cooperativity between intracellular calcium domains from adjacent channels, as suggested by others (Matveev et al., 2011; Schneggenburger et al., 2012).

In order to convert channel density and mobility into more physiological parameters, we calculated the P_r of readily releasable vesicles (RRVs; for parameters see Experimental Procedures). P_r depended on channel density and reached maximum in a surface of 0.09 μm² with one RRV and channel densities between 220 and 300 channels per μm² (Figures 4C and 4D). Allowing repositioning of channels over time resulted in a graded increase in P_r, which started at much lower channel densities. Channel mobility is particularly important for small synapses, where channel numbers are low and diffusion of channels induces high variability of P_r indicated by large standard deviations. Such variability of P_r has been reported for hippocampal synapses even along one axon (Ermolyuk et al., 2012). Immobilizing channels in a random distribution caused a steep change in P_r (Figure 4D). Reducing channel mobility similar as measured for BAPTA-AM-loaded cells induced a similar shift of P_r as for statically distributed channels. Increasing RRVs (5–10) shifted the P_r curve toward lower channel densities but kept variability of P_r for particular channel densities (Figure S4D). This modeling approach supports our hypothesis that a dynamic arrangement within the presynaptic membrane optimizes the density of VDCCs required for a given P_r. It indicates that mobile VDCCs equalize P_r for each individual synaptic vesicle independent from the positioning of the vesicle itself, which may modulate short-term plasticity.

DISCUSSION

Using sptPALM we could show that about 60% of presynaptic Ca^{2+} channels in hippocampal neurons are mobile yet confined within AZs. While we cannot rule out that the immobile fraction represents VDCCs tethered to SVs, this interpretation can hardly be reconciled with our finding that channel mobility was unaffected by KCl-induced changes in AZ membrane topography. In fact, loose channel-sensor coupling prevails at hippocampal synapses that harbor similar numbers of $Ca_v2.1$ and $Ca_V2.2$ channels (Ermolyuk et al., 2013; Vyleta and Jonas, 2014). Consistently, we found that the mobility is very similar for both channel types and does not mirror their differential assignment to nano- or microscale coupling at calyx of Held synapses (Fedchyshyn and Wang, 2005).

Limited by image acquisition frequency and duration, we cannot discriminate whether immobile and mobile channels represent separate subpopulations or temporal fluctuations of individual channels as predicted by our model. Immobilization within the AZ could reflect short-term nanoscale coupling with SVs or tight interactions with CAZ proteins. Various interactions between presynaptic VDCCs and scaffold proteins are known but some are mutually exclusive or involve discrete channel variants only (Davydova et al., 2014; Han et al., 2011; Kaeser et al., 2011; Liu et al., 2011; Maximov et al., 1999). The availability of scaffold proteins may be limited due to their engagement in
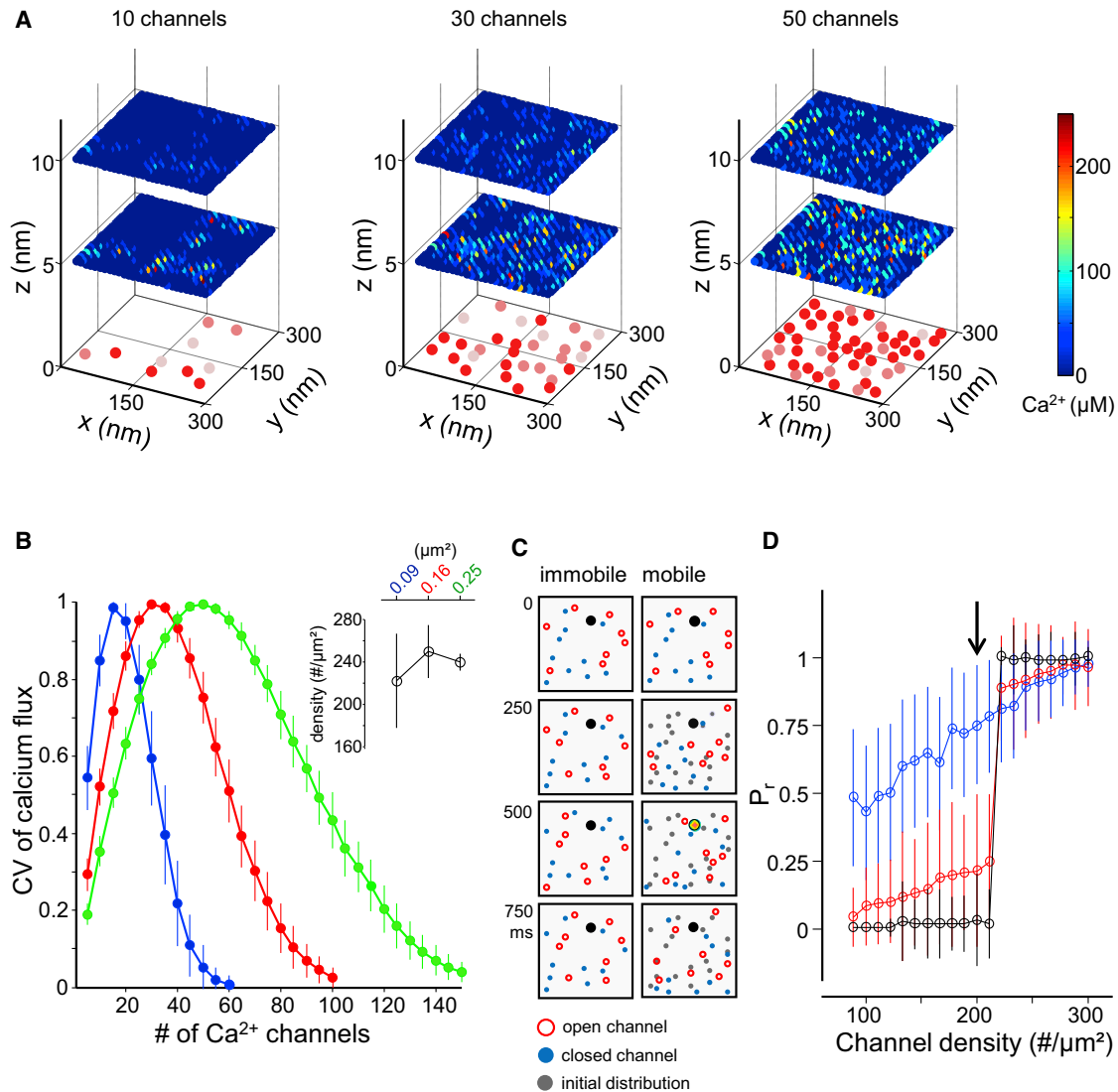
Figure 4. Modeling of Calcium Fluctuations as Function of Channel Number and Mobility

(A) Impact of channel density on intracellular calcium fluctuations at 5 and 10 nm distances from the membrane. Channel dynamics is color coded for three ranges of diffusion coefficient (gray, $D > 0.01$ $\mu m^2/s$; pink, $D = 0.001–0.01$ $\mu m^2/s$; red, $D < 0.001$ $\mu m^2/s$). $[Ca^{2+}]_i$ is color coded as indicated in the scale bar from 0 to 200 μM. (B) The CV for $[Ca^{2+}]_i$ fluctuations plotted against channel numbers within depicted areas of 300×300 nm (blue), 400×400 nm (red), 500×500 nm (green). A median diffusion coefficient of 0.02 $\mu m^2/s$ was assumed and channel open probability set to 0.5; for other parameters, see Supplemental Information. Inset shows channel density at maximal calcium variability versus AZ size. (C) Within a 300×300 nm area, one vesicle (black spot) was randomly placed 5 nm above the membrane. Channel distribution was monitored for static and mobile channel populations at time points as indicated and triggered for activation (see Supplemental Information for parameters). A colored vesicle indicates successful release due to random rearrangement of channels. (D) P_r plotted against channel density for populations of mobile channels (blue), immobile channels (black), or reduced mobility in presence of BAPTA-AM (red). Note that the sudden jump of the P_r is caused by the parameter of one RRV (see also Supplemental Information for parameters). Arrow indicates the density corresponding to the example distributions in (C). Points represent mean $P_r \pm$ SD of 100 iterations for given densities.

competing interactions. Otherwise identical channels may therefore be embedded differently within a given AZ. Consistent with previous observations (Cao and Tsien, 2010), we found a prominent Ca$_V$2.1 splice variant, which lacks established RIM/Mint1- and RBP-binding motifs (Chaudhuri et al., 2004; Davydova et al., 2014) to compete with endogenous channels for synaptic localization. For the mobile fractions of Ca$_V$2.1 and Ca$_V$2.2 channels, we calculated r_{conf} above 100 nm. Presuming a stretched conformation, the cytoplasmic tails of VDCCs (Wong et al., 2014) can explore a substantial area of the AZ while being linked to the CAZ. We used a modeling approach to assess the impact of this degree of freedom on P_r. At low channel densities, P_r increase with channel mobility. Same time channel density is predicted to reciprocally affect mobility. Thus, to ensure a certain P_r, the number of synaptic VDCCs may be kept low if their mobility is high enough. Our data suggest that the channel density is

optimized to the size of the AZ, keeping the majority of channels mobile. Accordingly, increased channel expression did not result in higher synaptic channel density. In addition, the immobilizing effect of BAPTA suggests that next to changing intracellular Ca^{2+} transients, channel positioning contributes to the P_r-reducing effect of BAPTA. Following this principle, non-uniform channel density across an AZ is counterbalanced by local mobility changes, resulting in an AZ-wide homogeneous contribution of VDCCs to P_r. Clustering of synaptic VDCCs within AZs has been detected by immuno-EM (Holderith et al., 2012; Indriati et al., 2013) in different synapses and was consistent with calculating realistic P_r (Ermolyuk et al., 2013). In contrast, immunogold labeling for Rim1/2 revealed a more uniform distribution for these VDCC-binding CAZ proteins (Holderith et al., 2012). Snapshots from mobile channel simulations occasionally appear cluster-like but reflect states of random distribution (Figure S4B). Our model suggests that the fractions of mobile and immobile channels are transient within the AZ, collectively represented as fractions of immobile and mobile channels within the experiments.

An obvious question is whether channel mobility is a fixed parameter for a given type of synapse or is subject to plasticity-related modulations. Our Ca^{2+} chelation experiments suggest the latter, demonstrating that reduced baseline levels of free $[Ca^{2+}]_i$ lead to a significant decrease in channel mobility. Syntaxin-1A behaved oppositely arguing against a generic effect. Baseline $[Ca^{2+}]_i$ can be regulated via signaling through G protein-coupled receptors, altered Ca^{2+} buffering, or extrusion. VDCCs themselves can add to baseline $[Ca^{2+}]_i$ in response to elevated resting potentials, thereby considerably increasing P_r (Awatramani et al., 2005). This raises the interesting possibility of a feedforward mechanism by which an increased rate of spontaneous VDCC opening within AZs translates into enhanced channel mobility and thus, according to our results, enhanced P_r. In view of the reported size of an intracellular calcium domain caused by single channel opening, which is tuned by endogenous calcium binding proteins (Tadross et al., 2013), the observed dynamics seem to be even more relevant. The dynamics of stochastically opening Ca^{2+} channels also offers a mechanism for the substantial contribution of high voltage-gated calcium channels to spontaneous transmitter release (Ermolyuk et al., 2013; Williams et al., 2012), in particular when considering the rather stable positioning of docked and primed vesicles in the presynaptic membrane (Lee et al., 2012; Lemke and Klingauf, 2005). To what extent channel densities vary between terminals remains to be explored, but in light of our study high channel densities could account for the nanodomain coupling observed in several synapses (Bucurenciu et al., 2008; Schmidt et al., 2013).

This study uncovers the existence and potential relevance of ongoing channel fluctuations within AZs. Regulatory modes that truly alter local synaptic channel densities rather than mean channel numbers remain to be identified. Our attempt to increase local synaptic channel density by co-expressing tagged $\alpha1$ subunits with $\alpha2\delta1$ led to increased synaptic VDCC numbers accompanied by enlargement of the CAZ. This observation is in accordance with the linear scaling of various presynaptic proteins with AZ size (Holderith et al., 2012; but see Hoppa et al., 2012). As an important new facet, we propose that VDCCs, beyond their documented permissive role in presynapse assembly at neuromuscular junctions (Chen et al., 2011), can play an instructive role in scaling AZs at hippocampal synapses. In addition, the variation of the distance between channel and sensor within very short timescales may introduce variability to short-term plasticity. Hence, differential effects of BAPTA could be interpreted as different modes of a dynamic interplay between calcium channel and calcium sensor (Vyleta and Jonas, 2014). The proposed equilibration of individual P_r might contribute to short-term plasticity changes, tuned by the dynamics of VDCC in the presynaptic compartment. Apart from synapses, mobility of VDCCs may play a role in modulation of the intrinsic excitability of neurons by adjusting the interplay between calcium channels and calcium-activated potassium channels.

EXPERIMENTAL PROCEDURES

Cell Culture

The experiments were conducted in primary hippocampal rat neurons prepared from embryonic Wistar rats (embryonic day 18) as described (Davydova et al., 2014). The detailed procedure and methods of transfection are described in detail in Supplemental Experimental Procedures.

Plasmids

Expression constructs for tagged VDCC $\alpha1$, $\alpha2\delta1$, and $\beta3$ subunits were generated by standard cloning strategies or kindly provided by various colleagues (see Supplemental Experimental Procedures).

Life Imaging

sptPALM experiments were conducted as described (Manley et al., 2008) using mEOS2-tagged constructs. Acquisition and analysis are described in detail in Supplemental Experimental Procedures.

Statistics

Statistical values are given as median with interquartile range (IQR) or mean ± SEM unless stated otherwise (see Supplemental Experimental Procedures for details).

SUPPLEMENTAL INFORMATION

Supplemental Information includes Supplemental Experimental Procedures and four figures and can be found with this article online at http://dx.doi.org/10.1016/j.neuron.2015.03.050.

REFERENCES

Awatramani, G.B., Price, G.D., and Trussell, L.O. (2005). Modulation of transmitter release by presynaptic resting potential and background calcium levels. Neuron 48, 109–121.

Borst, J.G., and Sakmann, B. (1996). Calcium influx and transmitter release in a fast CNS synapse. Nature *383*, 431–434.

Bucurenciu, I., Kulik, A., Schwaller, B., Frotscher, M., and Jonas, P. (2008). Nanodomain coupling between Ca2+ channels and Ca2+ sensors promotes fast and efficient transmitter release at a cortical GABAergic synapse. Neuron *57*, 536–545.

Cao, Y.Q., and Tsien, R.W. (2010). Different relationship of N- and P/Q-type Ca2+ channels to channel-interacting slots in controlling neurotransmission at cultured hippocampal synapses. J. Neurosci. *30*, 4536–4546.

Catterall, W.A. (1999). Interactions of presynaptic Ca2+ channels and snare proteins in neurotransmitter release. Ann. N Y Acad. Sci. *868*, 144–159.

Chaudhuri, D., Chang, S.Y., DeMaria, C.D., Alvania, R.S., Soong, T.W., and Yue, D.T. (2004). Alternative splicing as a molecular switch for Ca2+/calmodulin-dependent facilitation of P/Q-type Ca2+ channels. J. Neurosci. *24*, 6334–6342.

Chen, J., Billings, S.E., and Nishimune, H. (2011). Calcium channels link the muscle-derived synapse organizer laminin β2 to Bassoon and CAST/Erc2 to organize presynaptic active zones. J. Neurosci. *31*, 512–525.

Davydova, D., Marini, C., King, C., Klueva, J., Bischof, F., Romorini, S., Montenegro-Venegas, C., Heine, M., Schneider, R., Schröder, M.S., et al. (2014). Bassoon specifically controls presynaptic P/Q-type Ca(2+) channels via RIM-binding protein. Neuron *82*, 181–194.

Di Biase, V., Tuluc, P., Campiglio, M., Obermair, G.J., Heine, M., and Flucher, B.E. (2011). Surface traffic of dendritic CaV1.2 calcium channels in hippocampal neurons. J. Neurosci. *31*, 13682–13694.

Eggermann, E., Bucurenciu, I., Goswami, S.P., and Jonas, P. (2012). Nanodomain coupling between Ca^{2+} channels and sensors of exocytosis at fast mammalian synapses. Nat. Rev. Neurosci. *13*, 7–21.

Ermolyuk, Y.S., Alder, F.G., Henneberger, C., Rusakov, D.A., Kullmann, D.M., and Volynski, K.E. (2012). Independent regulation of basal neurotransmitter release efficacy by variable Ca^{2+} influx and bouton size at small central synapses. PLoS Biol. *10*, e1001396.

Ermolyuk, Y.S., Alder, F.G., Surges, R., Pavlov, I.Y., Timofeeva, Y., Kullmann, D.M., and Volynski, K.E. (2013). Differential triggering of spontaneous glutamate release by P/Q-, N- and R-type Ca2+ channels. Nat. Neurosci. *16*, 1754–1763.

Fedchyshyn, M.J., and Wang, L.Y. (2005). Developmental transformation of the release modality at the calyx of Held synapse. J. Neurosci. *25*, 4131–4140.

Han, Y., Kaeser, P.S., Südhof, T.C., and Schneggenburger, R. (2011). RIM determines Ca^{2+} channel density and vesicle docking at the presynaptic active zone. Neuron *69*, 304–316.

Holderith, N., Lorincz, A., Katona, G., Rózsa, B., Kulik, A., Watanabe, M., and Nusser, Z. (2012). Release probability of hippocampal glutamatergic terminals scales with the size of the active zone. Nat. Neurosci. *15*, 988–997.

Hoppa, M.B., Lana, B., Margas, W., Dolphin, A.C., and Ryan, T.A. (2012). α2δ expression sets presynaptic calcium channel abundance and release probability. Nature *486*, 122–125.

Indriati, D.W., Kamasawa, N., Matsui, K., Meredith, A.L., Watanabe, M., and Shigemoto, R. (2013). Quantitative localization of Cav2.1 (P/Q-type) voltage-dependent calcium channels in Purkinje cells: somatodendritic gradient and distinct somatic coclustering with calcium-activated potassium channels. J. Neurosci. *33*, 3668–3678.

Kaeser, P.S., Deng, L., Wang, Y., Dulubova, I., Liu, X., Rizo, J., and Südhof, T.C. (2011). RIM proteins tether Ca2+ channels to presynaptic active zones via a direct PDZ-domain interaction. Cell *144*, 282–295.

Lee, S., Jung, K.J., Jung, H.S., and Chang, S. (2012). Dynamics of multiple trafficking behaviors of individual synaptic vesicles revealed by quantum-dot based presynaptic probe. PLoS ONE *7*, e38045.

Lemke, E.A., and Klingauf, J. (2005). Single synaptic vesicle tracking in individual hippocampal boutons at rest and during synaptic activity. J. Neurosci. *25*, 11034–11044.

Li, L., Bischofberger, J., and Jonas, P. (2007). Differential gating and recruitment of P/Q-, N-, and R-type Ca2+ channels in hippocampal mossy fiber boutons. J. Neurosci. *27*, 13420–13429.

Liu, K.S., Siebert, M., Mertel, S., Knoche, E., Wegener, S., Wichmann, C., Matkovic, T., Muhammad, K., Depner, H., Mettke, C., et al. (2011). RIM-binding protein, a central part of the active zone, is essential for neurotransmitter release. Science *334*, 1565–1569.

Manley, S., Gillette, J.M., Patterson, G.H., Shroff, H., Hess, H.F., Betzig, E., and Lippincott-Schwartz, J. (2008). High-density mapping of single-molecule trajectories with photoactivated localization microscopy. Nat. Methods *5*, 155–157.

Matveev, V., Bertram, R., and Sherman, A. (2011). Calcium cooperativity of exocytosis as a measure of Ca^2+ channel domain overlap. Brain Res. *1398*, 126–138.

Maximov, A., Südhof, T.C., and Bezprozvanny, I. (1999). Association of neuronal calcium channels with modular adaptor proteins. J. Biol. Chem. *274*, 24453–24456.

Meinrenken, C.J., Borst, J.G., and Sakmann, B. (2002). Calcium secretion coupling at calyx of held governed by nonuniform channel-vesicle topography. J. Neurosci. *22*, 1648–1667.

Mercer, A.J., Chen, M., and Thoreson, W.B. (2011). Lateral mobility of presynaptic L-type calcium channels at photoreceptor ribbon synapses. J. Neurosci. *31*, 4397–4406.

Reid, C.A., Clements, J.D., and Bekkers, J.M. (1997). Nonuniform distribution of Ca2+ channel subtypes on presynaptic terminals of excitatory synapses in hippocampal cultures. J. Neurosci. *17*, 2738–2745.

Ribrault, C., Reingruber, J., Petković, M., Galli, T., Ziv, N.E., Holcman, D., and Triller, A. (2011). Syntaxin1A lateral diffusion reveals transient and local SNARE interactions. J. Neurosci. *31*, 17590–17602.

Schmidt, H., Brachtendorf, S., Arendt, O., Hallermann, S., Ishiyama, S., Bornschein, G., Gall, D., Schiffmann, S.N., Heckmann, M., and Eilers, J. (2013). Nanodomain coupling at an excitatory cortical synapse. Curr. Biol. *23*, 244–249.

Schneggenburger, R., Han, Y., and Kochubey, O. (2012). Ca(2+) channels and transmitter release at the active zone. Cell Calcium *52*, 199–207.

Scholz, K.P., and Miller, R.J. (1995). Developmental changes in presynaptic calcium channels coupled to glutamate release in cultured rat hippocampal neurons. J. Neurosci. *15*, 4612–4617.

Scimemi, A., and Diamond, J.S. (2012). The number and organization of Ca2+ channels in the active zone shapes neurotransmitter release from Schaffer collateral synapses. J. Neurosci. *32*, 18157–18176.

Tadross, M.R., Tsien, R.W., and Yue, D.T. (2013). Ca2+ channel nanodomains boost local Ca2+ amplitude. Proc. Natl. Acad. Sci. USA *110*, 15794–15799.

Vyleta, N.P., and Jonas, P. (2014). Loose coupling between Ca2+ channels and release sensors at a plastic hippocampal synapse. Science *343*, 665–670.

Williams, C., Chen, W., Lee, C.H., Yaeger, D., Vyleta, N.P., and Smith, S.M. (2012). Coactivation of multiple tightly coupled calcium channels triggers spontaneous release of GABA. Nat. Neurosci. *15*, 1195–1197.

Wong, F.K., Nath, A.R., Chen, R.H., Gardezi, S.R., Li, Q., and Stanley, E.F. (2014). Synaptic vesicle tethering and the CaV2.2 distal C-terminal. Front. Cell. Neurosci. *8*, 71.

Mobility of Calcium Channels
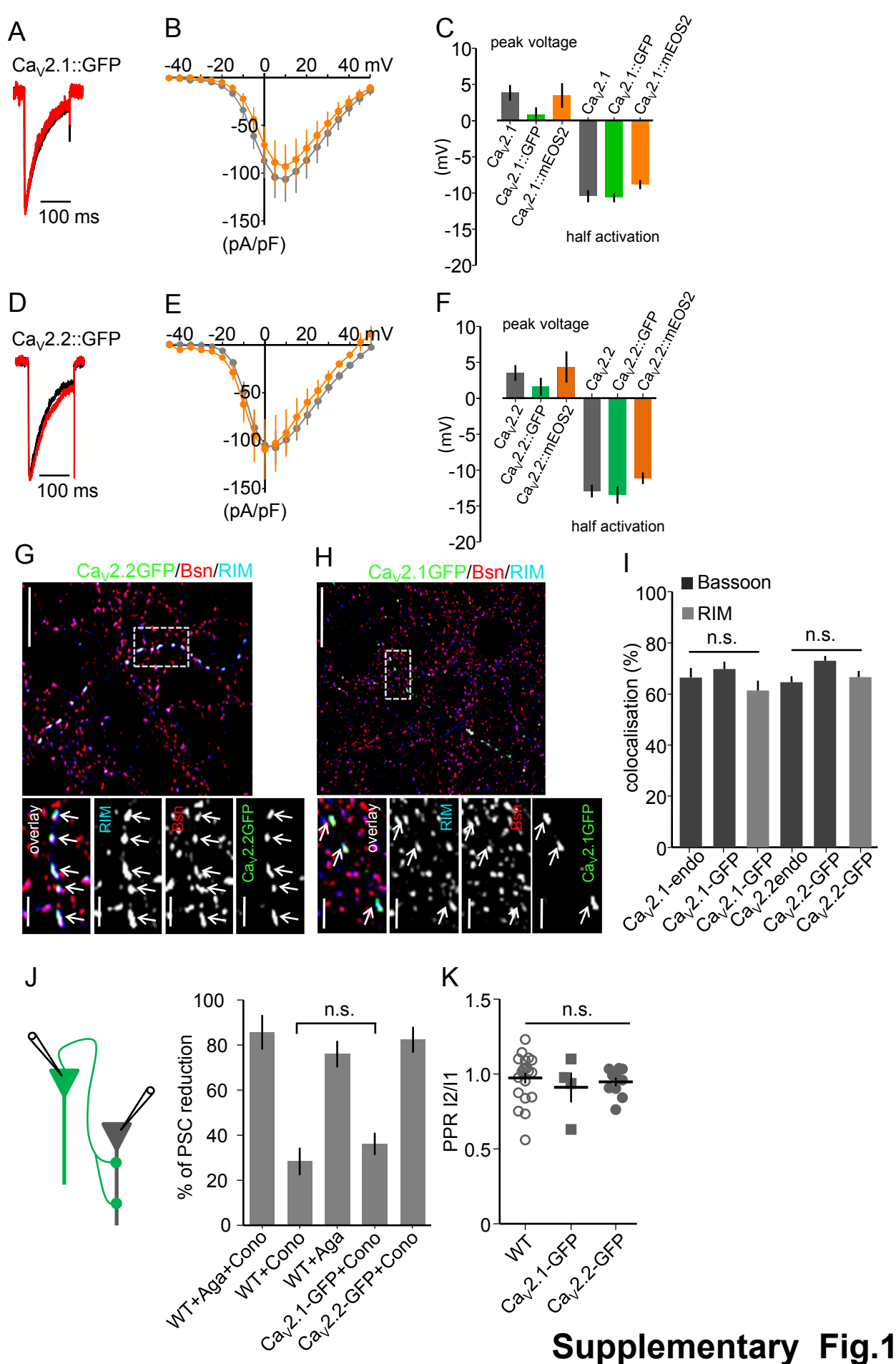
in the Presynaptic Membrane

Romy Schneider, Eric Hosy, Johannes Kohl, Julia Klueva, Daniel Choquet, Ulrich Thomas, Andreas Voigt, and Martin Heine

Supplementary information
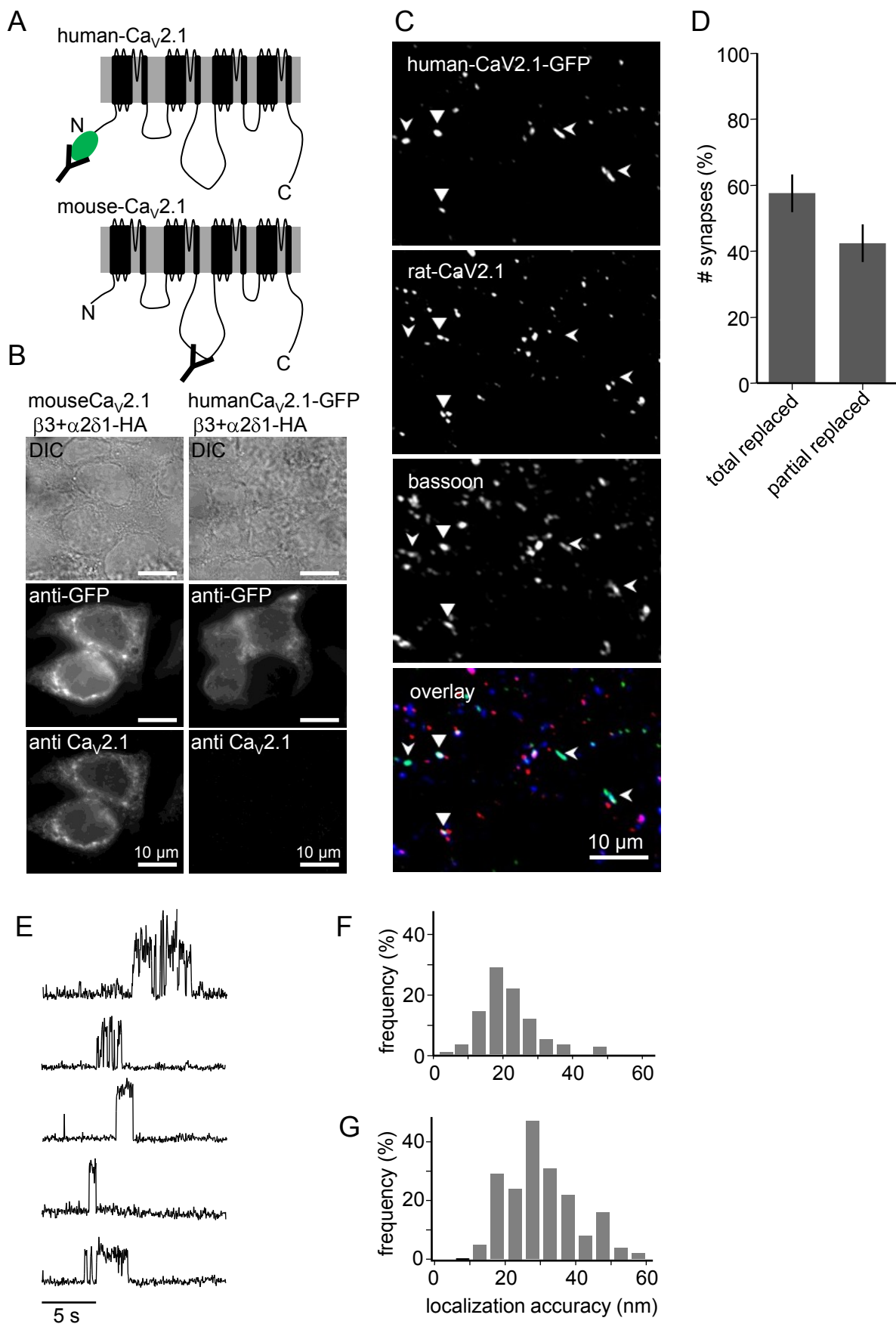
supplementary Figures 1-4

Supplementary Fig.1

Supplementary Figure 1:

S1 related to Figure 1, 2 and 3

Functional characterisation and synaptic expression of N-terminal tagged Ca$_V$2.1 and Ca$_V$2.2 channels

(A) Barium currents elicited by a depolarisation step from -90 mV to 0 mV for 150 ms in HEK-cells transfected with Ca$_V$2.1 + β3 + α2δ1 (black) or Ca$_V$2.1::GFP + β3 + α2δ1 (red). **(B)** IV relationship for Ca$_V$2.1 + β3 + α2δ1 (grey) and Ca$_V$2.1::EOS + β3 + α2δ1 (orange) displayed as current density at different membrane potentials, values are not corrected for liquid junction potential (n = 13 for Ca$_V$2.1 + β3 + α2δ1 and n = 16 for Ca$_V$2.1::mEOS2 + β3 + α2δ1). **(C)** Calculated peak voltage and half maximal activation for Ca$_V$2.1 (grey, n = 20) Ca$_V$2.1::GFP (green, n = 13) and Ca$_V$2.1::EOS (orange, n = 9) do not differ significantly (one-way ANOVA). **(D)** Barium currents elicited by a transient depolarisation step from -90 mV to 0 mV for 150 ms in HEK-cells transfected with of Ca$_V$2.2 + β3 + α2δ1 (black) and Ca$_V$2.2::GFP + β3 + α2δ1 (red). **(E)** IV relationship for Ca$_V$2.2 + β3 + α2δ1 (grey) and Ca$_V$2.2::mEOS2 + β3 + α2δ1 (orange) displayed as current density at different membrane potentials, values are not corrected for liquid junction potential (n = 22 for Ca$_V$2.2 + β3 + α2δ1 and n = 5 for Ca$_V$2.2::mEOS2 + β3 + α2δ1). **(F)** Calculated peak voltage and half maximal activation for Ca$_V$2.2 (grey, n = 17), Ca$_V$2.2::GFP (green, n = 10) and Ca$_V$2.2::mEOS2 (orange, n = 9) do not differ significantly (one-way ANOVA). **(G)** Overlay of immunofluorescence images for Ca$_V$2.1::GFP (green)/bassoon (red)/RIM (blue). Boxed areas are enlarged to illustrate the co-localisation of Ca$_V$2.1::GFP with the two presynaptic scaffold proteins, RIM and Bassoon. Arrows indicate localised clusters for all three proteins. **(H)** Same experiment as in **(G)**, but for Ca$_V$2.2::GFP. Dimension of the scale bars are 10 μm for the overlay pictures and 2 μm for the enlarged boxed areas for both (H) and (G). **(I)** Relative co-localisation for endogenous and overexpressed Ca$_V$2.1 or Ca$_V$2.2 with Bassoon and RIM, differences are not significant (Bassoon: n$_{CaV2.1endo}$ = 2929 synapses, n$_{CaV2.1::GFP}$ = 1516 synapses, n$_{CaV2.2endo}$ = 2783 synapses, n$_{CaV2.2::GFP}$ = 510 synapses; RIM: n$_{CaV2.1::GFP}$ = 1157 synapses, n$_{CaV2.2::GFP}$ = 719 synapses). Scale bars in (G) and (H) represent 10 μM for the overlay and 2 μM for the zoomed area. **(J)** Postsynaptic currents recorded from coupled pairs of cultured hippocampal neurons, expressing Ca$_V$2.1::GFP or Ca$_V$2.2::GFP were compared to the wild type situation. First, contribution of expressed channel isoforms was measured by cumulative block of Ca$_V$2.1 and Ca$_V$2.2 (n = 3) or single block of Ca$_V$2.2 with 1 μM ω-Conotoxin GIVA (n = 10) and Ca$_V$2.1 with 0.5 μM ω-Agatoxin IVA (n = 11). Expression of Ca$_V$2.1::GFP did not alter the synaptic fraction of Ca$_V$2.1 within the transfected synapse (n = 5), whereas expression of Ca$_V$2.2::GFP (n = 4) led to a complete dominance of Ca$_V$2.2 channels within the synapse as revealed by enhanced sensitivity to ω-Conotoxin. **(K)** Paired-pulse ratio upon stimulations with an interval of 50 ms were not significantly different between non-transfected (n = 16) and transfected neurons (Ca$_V$2.1::GFP, n = 4; Ca$_V$2.2::GFP, n = 10). All quantified data are given as mean ± SEM.

A

human-Ca$_V$2.1

N

mouse-Ca$_V$2.1

N

C

B

mouseCa$_V$2.1
β3+α2δ1-HA

humanCa$_V$2.1-GFP
β3+α2δ1-HA

DIC

DIC

anti-GFP

anti-GFP

anti Ca$_V$2.1

anti Ca$_V$2.1

10 μm

10 μm

C

human-CaV2.1-GFP

rat-CaV2.1

bassoon

overlay

10 μm

D

synapses (%)

total replaced

partial replaced

E

5 s

F

frequency (%)

localization accuracy (nm)

G

frequency (%)

localization accuracy (nm)

Supplementary Figure 2

Supplementary Figure 2:

S2 related to Figure 3 and experimental procedure (S2E, F; sptPALM)

Expression level of tagged calcium channels in presynaptic boutons and characterisation of fluorescence signals from mEOS2 tagged calcium channels

(A) Schematic representation of binding domains for anti GFP-antibody and the rodent-specific antibody against the II-III intracellular loop in $Ca_V2.1$. **(B)** Images of HEK-cells expressing mouse $Ca_V2.1$::GFP + $\beta3$ + $\alpha2\delta1$::HA or the human isoform of $Ca_V2.1$::GFP + $\beta3$ + $\alpha2\delta1$::HA show clear anti-GFP labelling for both, whereas anti-$Ca_V2.1$ immunoreactivity is restricted to the mouse isoform. Scale bar represents 10 μm. **(C)** Co-labelling of endogenous $Ca_V2.1$ channel population and expressed human $Ca_V2.1$::GFP together with Bassoon uncover two populations of synapses, one expressing only human $Ca_V2.1$::GFP (open arrows) and a second population expressing human $Ca_V2.1$::GFP and the endogenous rat $Ca_V2.1$::GFP. Scale bar 10 μm. **(D)** Percentages of synapses expressing only human $Ca_V2.1$::GFP (total replacement) versus synapses with both endogeneous $Ca_V2.1$ and human $Ca_V2.1$::GFP, 10 DIV after transfection (2 cultures, 739 synapses). **(E)** Examples of fluorescence events of single mEOS2-tagged $Ca_V2.1$-channels expressed in COS7-cells. **(F)** Distribution of localisation accuracy calculated for $Ca_V2.1$::mEOS2 channels in fixed cells (n = 119), mean accuracy 21.4 ± 4 nm. **(G)** Distribution of localization accuracy of $Ca_V2.1$::mEOS2 channels expressed in hippocampal neurons 14 DIV, mean accuracy 27.7 ± 10 nm (n = 100). All quantified data are given as mean ± SEM.
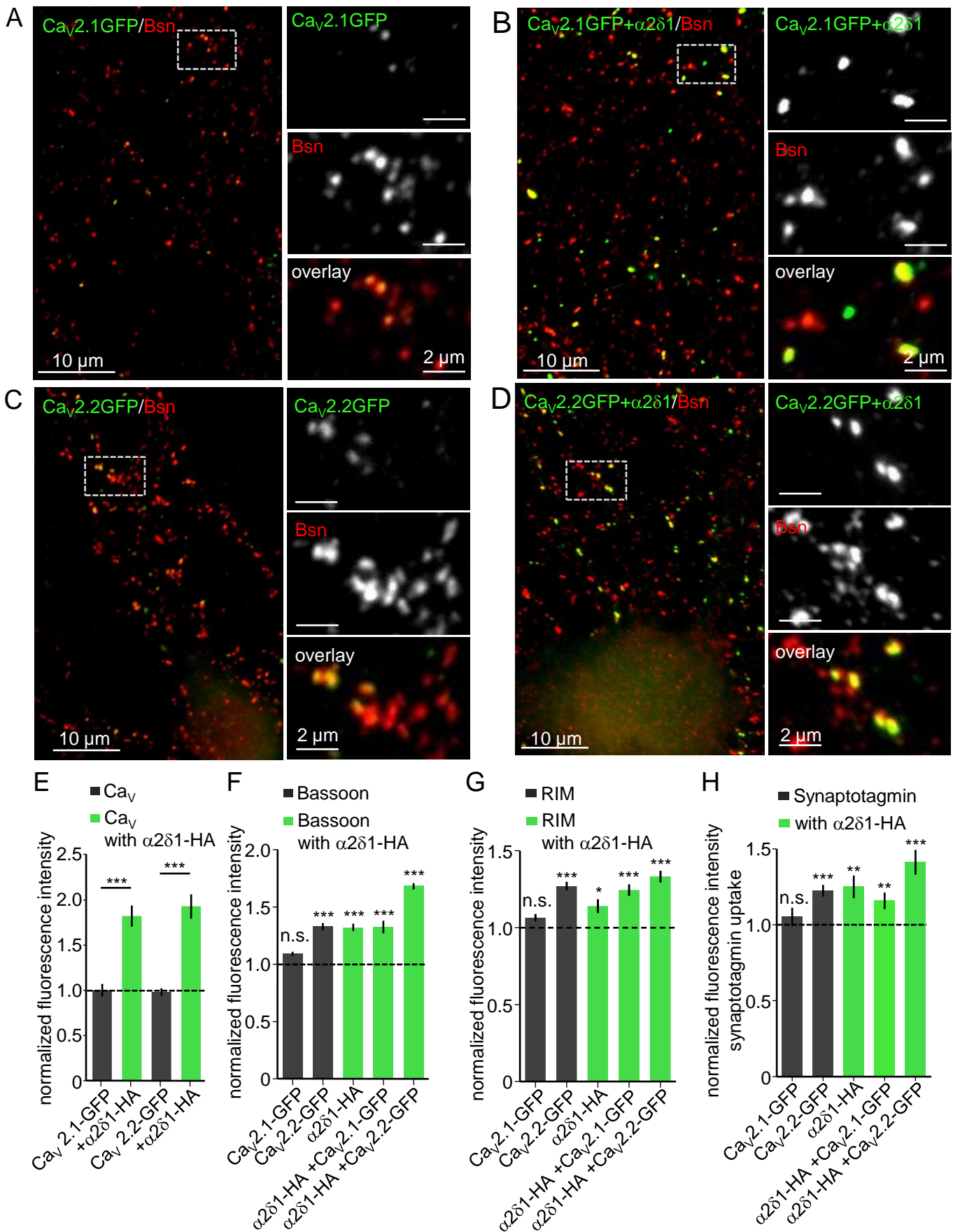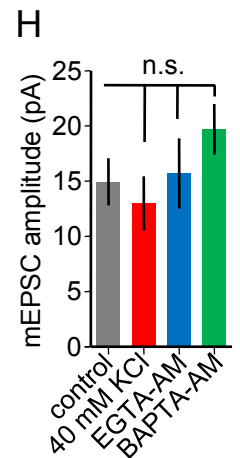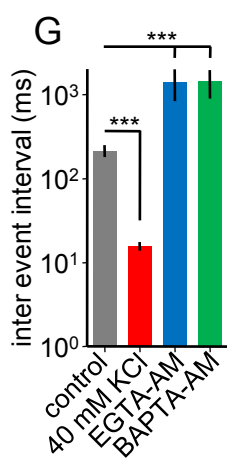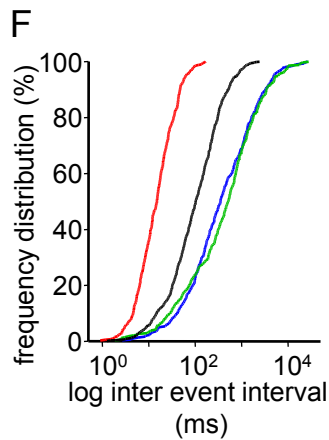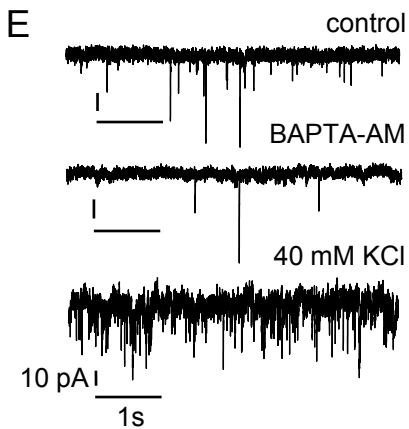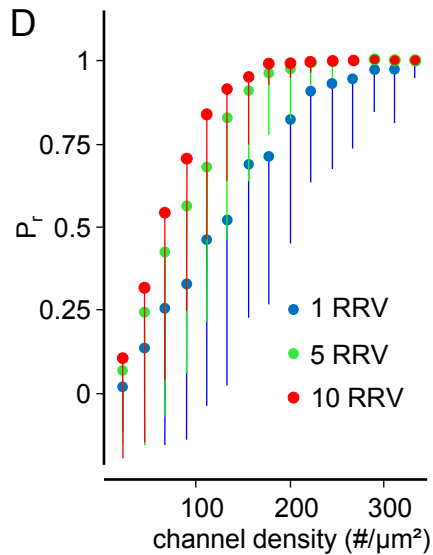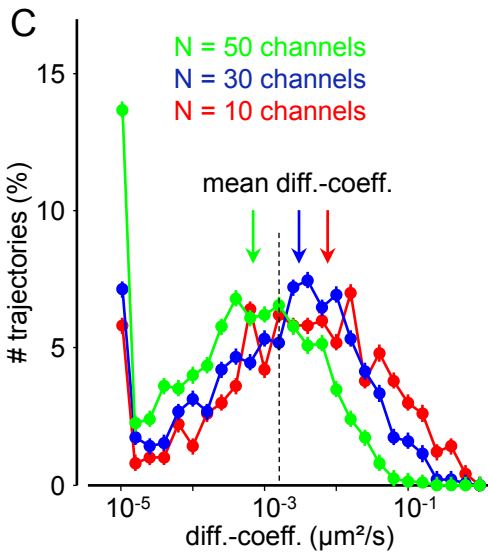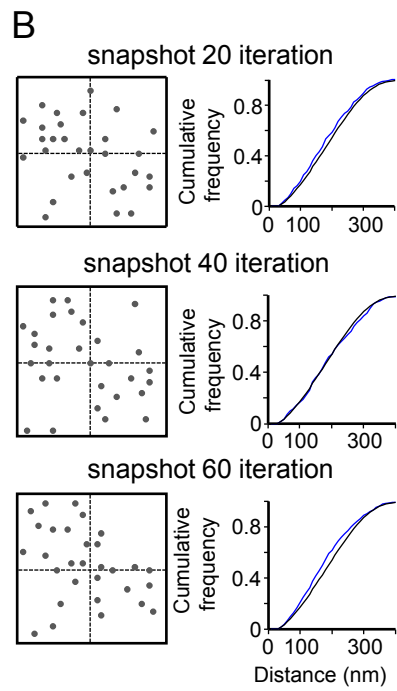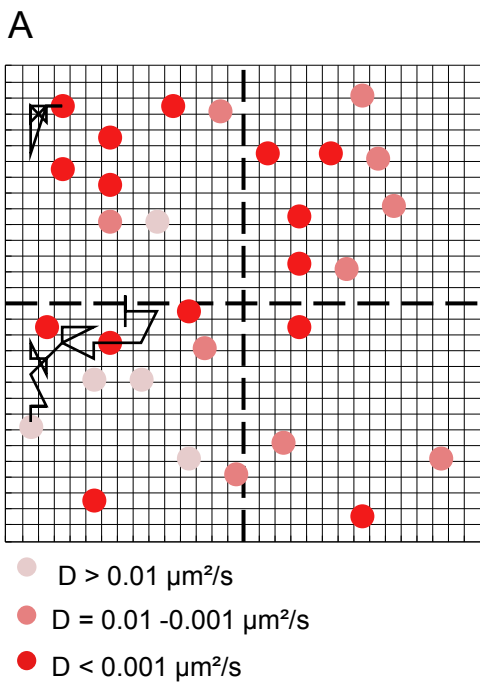
Supplementary Figure 3

Supplementary Figure 3:

S3 related to Figure 3

Changes in expression level of calcium channels, Bassoon and RIM induced by expression of tagged calcium channels with and without the $\alpha2\delta1$-subunit.

(A-D) Fluorescence detection of tagged Ca_V2::GFP channels and the presynaptic scaffold protein Bassoon in cultured hippocampal neurons with (B, D) or without (A, C) co-expression of HA-$\alpha2\delta1$. Insets display synaptic clusters of $Ca_V2.1$::GFP or $Ca_V2.2$::GFP with Bassoon next to synapses from non-transfected cells with Bassoon clusters only. Scale bars represent 10 μm for overviews and 2 μm for zoomed regions. **(E)** Quantification of fluorescence intensity for N-terminal tagged calcium channels with and without $\alpha2\delta1$-subunit ($Ca_V2.1$::GFP: n = 1661 synapses, + $\alpha2\delta1$: n = 1854 synapses; $Ca_V2.2$::GFP: n = 634 synapses, + $\alpha2\delta1$: n = 1555 synapses, from 3-4 independent cultures 14-21 DIV). **(F)** Fluorescence intensities for Bassoon in the presence of different combinations of channel subunits, normalized to intensities in non-transfected cells; stastistical analysis by one-way ANOVA test followed by a Dunnett-test, data derived from 2-3 independent cultures 14-21 DIV ($Ca_V2.1$::GFP/Bassoon n = 787 synapses, $Ca_V2.2$::GFP/Bassoon n = 367 synapses, $\alpha2\delta1$::HA/Bassoon n = 239 synapses, $Ca_V2.1$::GFP + $\alpha2\delta1$::HA/Bassoon n = 137 synapses, $Ca_V2.2$::GFP + $\alpha2\delta1$::HA/Bassoon n = 1043 synapses). **(G)** Fluorescence intensities for RIM in the presence of different combinations of channel subunits, normalized to intensities in non-transfected cells; stastistical analysis by one-way ANOVA test followed by a Dunnett-test, data derived from 2-3 independent cultures 14-21 DIV ($Ca_V2.1$::GFP/RIM n = 1137 synapses, $Ca_V2.2$::GFP/RIM n = 600 synapses, $\alpha2\delta1$::HA/RIM n = 303 synapses, $Ca_V2.1$::GFP + $\alpha2\delta1$::HA/RIM n = 936 synapses, $Ca_V2.2$::GFP + $\alpha2\delta1$::HA/RIM n = 1436 synapses). **(H)** Activity dependent uptake of fluorescently labelled anti-synaptotagmin1 antibody incubated for 20 min at 37 °C. Anti-synaptotagmin1 fluorescence intensity is normalized to average uptake of non-transfected synapses within the same preparation, we compared for $\alpha2\delta1$::HA (5162 synapses); Cav2.2::GFP (2328 synapses); Cav2.2::GFP + $\alpha2\delta1$::HA (2328 synapses); Cav2.1::GFP (3263 synapses) and Cav2.1::GFP + $\alpha2\delta1$::HA (6663 synapses) from 2-3 independent cultures 14-21 DIV. All quantifications are given as mean ± SEM.

A

D > 0.01 μm²/s
D = 0.01 -0.001 μm²/s
D < 0.001 μm²/s

B

snapshot 20 iteration

snapshot 40 iteration

snapshot 60 iteration

Cumulative frequency

Distance (nm)

C

N = 50 channels
N = 30 channels
N = 10 channels

mean diff.-coeff.

trajectories (%)

diff.-coeff. (μm²/s)

D

P_r

1 RRV
5 RRV
10 RRV

channel density (#/μm²)

E

control

BAPTA-AM

40 mM KCl

10 pA

1s

F

frequency distribution (%)

log inter event interval (ms)

G

inter event interval (ms)

***

***

control
40 mM KCl
EGTA-AM
BAPTA-AM

H

mEPSC amplitude (pA)

n.s.

control
40 mM KCl
EGTA-AM
BAPTA-AM

Supplementary Figure 4

Supplementary Figure 4:

S4 related to Figure 4 and experimental procedures (S4E-G)

Illustrated model assumptions for assessing the impact of spatial confinement on the mobility of VDCCs/changes in synaptic activity under KCl depolarisation or intracellular calcium buffering

(A) Snapshot of the distribution of 30 channels within a 300 x 300 nm area starting with an initial diffusion coefficient of 0.02 µm²/s. Note the segregation in very low/immobile channels (labelled dark pink, diff.-coeff. < 0.001 µm²/s), mobile (labelled pink, diff.-coeff. = 0.001-0.01 µm²/s) and highly mobile (labelled red, diff.-coeff. > 0.01 µm²/s) channels, which is only caused by the spatial confinement over time. Indicated by the quadrant borders marked with dashed lines channels appear occasional clustered. **(B)** Three snapshots at different time-points of simulation are given to illustrate the variability in channel arrangements. Appearing tendencies of clusterisation of molecules are not different from random distribution as indicated in the cumulative distributions beside the examples. **(C)** Frequency distributions of diff.-coeff. within a defined membrane compartment (300x300 nm) for three different channel populations: 10 (red), 30 (blue) and 50 (green) channels. The increase in the immobile fraction as well as the left shift of the distribution indicates the effect of molecular crowding. The dashed line indicates the border for mobile and immobile fractions as used for the experimental data. Medians of the diffusion coefficients are indicated by arrows above the distributions. **(D)** Plotted are release probabilities (P_r) against channel density for different numbers of docked vesicles, as indicated one ready releasable vesicle (RRV, blue), five RRV (green) and ten RRV (red). Each curve represents the mean P_r ± SD calculated from 100 iterations for each density and vesicle number. **(E)** Example traces for mEPSCs under control conditions, after incubation with BAPTA-AM (20 µM for 20 min). **(F)** Cumulative distribution of inter event interval for 40 mM KCl (red), control (black) EGTA-AM (green) and BAPTA-AM (blue). **(G)** Mean ± SEM of interevent interval for the different conditions. **(H)** Mean ± SEM for mEPSC amplitude for the conditions as indicated. Data are from 2 independent cultures 14-16 DIV (control: 15 cells, KCl: 8 cells, EGTA-AM: 6 cells, BAPTA-AM: 7 cells). Differences between data were tested by one-way ANOVA followed by Bonferroni post-test, p < 0.0005 ***.

Supplementary experimental procedures

Cell culture/transfection

Dissociated primary rat hippocampal cultures were prepared from embryonic Wistar rats day E18 as described previously (Frischknecht et al., 2008). Briefly, cell suspensions obtained after dissociation with trypsin were plated onto poly-L-lysine (Sigma)-coated 18 mm glass coverslips (Menzel-Glaeser, Braunschweig, Germany) at a density of 30,000 cells per coverslip. After 1-2 h in Dulbecco's Modified Eagle Medium (DMEM) plus fetal bovine serum at 37 °C, five coverslips were transferred into a 35 mm dish containing a 70 - 80% confluent monolayer of astrocytes in neurobasal medium supplemented with B27 and 5 mM glutamine. Cultures were maintained at 37 °C in a humidified incubator with an atmosphere of 95% air and 5% CO_2. At 3 days in vitro (DIV) AraC was added to the cells to a final concentration of 1.4 μM.

Neurons were transfected at 4-5 DIV using the calcium phosphate method. Prior to transfection, cells were placed in a 12 well dish with 1 ml 37°C Optimem media (Life Technologies). To prepare the precipitate, 150 μl of transfection buffer in mM: 274 NaCl, 10 KCl, 1.4 Na_2HPO_4, 15 Glucose, 42 HEPES, pH 7.04-7.1 was added drop wise to a solution containing 5 μg of DNA and 250 mM $CaCl_2$, under gentle stirring. The resulting mix was placed for 20 min at RT; 60 μl of the mix was added per well, and neurons were placed in the incubator for 30 to 60 min. Medium was exchanged for 2 ml 37°C pre-warmed Neurobasal medium, followed by two times exchanging 1.5 ml. Finally, after this procedure cells were placed back in the stored dishes in conditioned culture media. Experiments were performed between 14 and 21 DIV.

Transient expression of tagged VDCCs in COS-7 cells or human embryonic kidney cells (HEK-293) was achieved by co-transfection of constructs for tagged α1-subunits together with β3- and α2δ1-encoding constructs at a 1:1:1 ratio using the FuGENE® X-tremeGENE 9 DNA transfection reagent (Roche) according to manufacturer's protocol. For comparison with non-tagged subunits we either transfected non-tagged subunit combinations in case of $Ca_V2.1$ or used a stable cell line expressing $Ca_V2.2$ (kindly provided by the lab of D. Lipcombe; (Lin et al., 2004)). Transiently transfected cells were measured 24-48 h after transfection. Current amplitudes >1 nA were considered to result from successful co-transfection of all three subunits (α1, β3 and α2δ1) as further confirmed by simultaneous detection of the GFP-tag fused to β3- and the extracellular HA epitope in α2δ1::HA (data not shown).

Plasmids/Molecular biology

Calcium channel α1-subunits used were mouse $Ca_V2.1$ (Addgene Plasmid 26578), human $Ca_V2.1$ (GenBank FJ040507), rat $Ca_V2.2$ (UniProtKB Q02294) and rabbit $Ca_V2.2$ (GenBank D14157). The N-terminal GFP labeled Ca_V2 constructs were described elsewhere (Szabo et al., 2006). Other calcium channel subunit cDNAs as β3 and α2δ1 were bought from Addgene (β3, Addgene 26574; α2δ1, Addgene 26575). For sptPALM experiments the N-terminal GFP was replaced by mEos2 using AvarI and RsrII restriction sites. The mEos2 cDNA was from Addgene (Plasmid 36236, generated by the lab of Robinson University of Delaware). AvarI and RsrII restriction sites were added by PCR. The extracellularly Human influenza hemagglutinin based tag (HA-tag) -labeled mouse α2δ1 construct

was a gift from the lab of Gerald Obermair. Shortly after the signal peptide a double HA-tag was inserted between Phe27 and Pro28. All generated constructs were verified by sequencing. mEOS2::syntaxin1A was a generous gift from Dr. F. Meunier (Queensland Brain Institute, Australia).

Electrophysiological recordings

Whole-cell patch-clamp recordings on HEK cells were performed 24-48h after transfection at room temperature (RT). Patch pipettes were pulled from borosilicate glass with a pipette resistance between 2 and 4 MΩ. The pipette solution contained in mM: 130 CsCl, 3 $MgCl_2$, 0.66 $CaCl_2$, 11.7 EGTA, 10 HEPES (pH 7.4, 310 mOsm). Prior to experiments, 1 mM ATP and 0.1 mM GTP were added and pH was readjusted to 7.2 to 7.3 with CsOH. The extracellular solution contained in mM: 140 NaCl, 10 $BaCl_2$, 1 $MgCl_2$, 10 HEPES, 10 D-(+)-Glucose, pH 7.4 adjusted by adding NaOH, the osmolarity was between 300-310 mOsm. Barium currents were recorded by the use of an EPC10 patch-clamp amplifier (HEKA, Germany) and registered by the use of patch-master software 2.7 (HEKA, Germany). Leak currents have been subtracted online using a p/4 protocol running before the voltage protocol to trigger channel activation. Data analysis was performed using FitMaster 2.69 (HEKA), IGOR Pro 5.0 (WaveMetrics, USA) and Prism 5.0 (GraphPad, USA) software.

Paired whole cell recordings in cultured primary hippocampal neurons were performed after 14-21 DIV and at least 7 days after transfection. Primary hippocampal cultures were constantly perfused with extracellular solution containing in mM: 145 NaCl, 2.5 KCl, 2 $MgCl_2$, 2 $CaCl_2$, 10 Hepes, and 10 D-glucose (pH 7.4 adjusted with NaOH). Patch pipettes from borosilicate glass had a pipette resistance of 3-5 MΩ when filled with the intracellular solution of the following composition: 140 K-gluconate, 1 $MgCl_2$, 2 $CaCl_2$, 4 NaATP, 10 EGTA, 10 HEPES, and 0.4 GTP (pH 7.25 adjusted with KOH). Only patches with a series resistances <15 MΩ were analyzed. The membrane potential was clamped to -60 mV for the postsynaptic cell. In the presynaptic (transfected cell) action potentials were evoked by current pulses of 500 pA amplitude, 1 ms duration and 50 ms interpulse interval. Only pairs with latency between action potential and peak of EPSC shorter than 4 ms were considered as directly coupled. To test the contribution of $Ca_V2.2$ and $Ca_V2.1$ channels to evoked postsynaptic currents (EPSCs) the specific calcium channel blockers ω-Conotoxin GVIA (1μM) and ω-Agatoxin IVA (400 nM), both from Alomone Labs, Jerusalem, Israel, were added to the bath solution. Perfusion was stopped before toxin application. Relative changes of EPSC amplitude were recorded 8 minutes after the application of the first and 8 minutes after the application of the second toxin. The order of toxin application was altered between experiments. Residual calcium currents were blocked by application of 100 μM $CdCl_2$ at the end of the experiment (data not shown).

In order to access Short-term synaptic plasticity paired pulse ratio (PPR) was calculated as ratio between the second EPSC and the first EPSC from at least 10 responses. For recordings cells were kept at 30-32 °C.

mEPSCs were measured with similar solutions and temperature in the presence of 1 μM TTX, 10 μM APV and 10μM Picrotoxin to isolate AMPAR mediated synaptic currents. Patches with a serious resistance < 10 MΩ were analyzed using synaptosoft minianalysis (USA).

Immunohistochemistry

Primary antibodies were either applied to live cells before fixation to access the surface population of proteins or to fixed and permeabilized cells to visualize the the total population of proteins. Live cell labelling was performed within cultured medium at 37°C and cells were fixed thereafter. As fixative we used 4 % paraformaldehyde (PFA) in phosphate buffered salt solution (PBS) for 5 min starting at 37 °C and permeabilized for 2 min with 0.3 % TritonX in PBS. Afterwards unspecific immune reactivity was blocked by washing cells three times 10 min with a washing buffer containing 10 % fetal calf serum (FCS), 25 mM Glycin and 2 % bovine serum albumin (BSA) in PBS. Primary and secondary antibodies were applied consecutively for 1 h at RT. After additional washing steps cells were mounted on glass slides with Mowiol. The following primary antibodies were used: rabbit anti-GFP 1:1000 (Molecular Probes, Cat.-Nr. A6455); mouse monoclonal anti-GFP 1:1000 (Roche, Cat.-Nr. 11814460001, clone 7.1 and 13.1); rat anti-HA 1:1000 (Roche, Cat.-Nr. 11867423001, clone 3F10); mouse anti-HA 1:1000 (Covance, Cat.-Nr. MMS-101P, clone 16B12); guinea pig anti-Bassoon 1:1000 (synaptic system, Cat.-Nr. 141004 polyclonal); rabbit anti-RIM1/2 1:2000 (synaptic system, Cat.-Nr. 140203 polyclonal); fluorescently labelled anti-Synaptotagmin live 1:200 (synaptic system, Cat.Nr. 105103C3 polyclonal); fluorescently labelled mouse anti-Synaptotagmin live 1:200 (synaptic system, Cat.-Nr. 105311CpH monoclonal); rabbit anti-Ca_V2.2 1:1000 (Alomone Labs, Cat.-Nr. ACC-002); rabbit anti Ca_V2.1 1:1000 (synaptic system, Cat.-Nr. 152103); and secondary fluorescently labelled antibodies Alexa 488-, Cy3-, Cy5-antibodies from Jackson ImmunoResearch Laboratories.

Image acquisition and analysis

Immunfluorescence images were either acquired on an upright microscope (Zeiss-Axio Imager A2, Germany) equipped with a PlanApochromat 63x/1.4 Oil objective (Zeiss, Germany), a Compact Light Source LQ-HXP 120 with a Mercury short arc reflector lamp (OSRAM HXP-R120W/45C Visitron Systems GmbH, Germany) and a CCD camera (CoolSNAP EZ, Photometrics, USA) under the control of VisiView software (Visitron Systems GmbH, Germany) or a confocal imaging setup based on a spinning disc mounted to a upright microscope (Olympus BX51WI). Here fluorescence signals were detected by an EM-CCD camera (Andor iXon 897D) controlled by IQ2-acquisition software (Andor, Ireland).

Acquired images were processed using MetaMorph software (Universal Imaging, USA). Synaptic puncta were defined as square regions of interest (ROI) with dimensions of about 0.9 x 0.9 μm around local intensity maxima using OpenView software (a gift from N.E. Ziv (Tsuriel et al., 2006)). Mean fluorescence intensities of transfected cells were normalized to the mean fluorescence intensities of non-transfected cells in the same region. Colocalisation of fluorescent spots was defined by matching ROI with the labelling for presynaptic calcium channels with scaffold proteins as Bassoon and RIM as quantified in Fig. S1I. The matched area was set to overlap at least 70 % to be considered as colocalised.

Quantification of the active zone size was performed by analyzing images acquired with a STED microscope (Leica TCS SP5). We imaged presynaptic Bassoon labeled with guinea pig anti-Bassoon antibody (synaptic system, Cat.Nr. 141004, polyclonal) and fluorescently labelled by anti-guinea pig ATTO 647N-conjugated secondary antibodies. Maximum projections of image stack where used to

determine the x-y dimension of the clusters by Gaussian fitting of the fluorescence signal. The fitting procedure is part of the MetaMorph based plugin PalmTracer also used for sptPALM analysis.

sptPALM

Cells were mounted in a Ludin chamber and imaged at 37°C using a TIRF microscope (IX81 microscope within an Xcellence system, Olympus, Germany). Laser lines were calibrated and adjusted individually by the use of the TIRF-multicolor condenser (Olympus, Germany). The microscope was equipped with a TIRF objective (100x 1.49 NA Olympus, Germany). Images were acquired using an Image EM C9100-13 digital monochrome back-thinned EM-CCD camera (Hamamatsu Photonics Germany). For photo-activation localization microscopy (PALM), cells expressing mEOS2-tagged constructs were photo-activated using a 405 nm laser and the resulting photo converted single-molecule fluorescence signal was excited with a 561 nm laser. Both lasers illuminated the sample simultaneously. In order to isolate the mEOS2 signal from auto fluorescence and background signals we used a triple beam splitter (zt UV-405/488/561, Chroma Technology Corp, USA) and Emission Bandpass filter (BP 605/40, Chroma Technology Corp, USA). The power was adjusted to keep the number of the stochastically activated molecules constant and well separated during the acquisition (405 laser used 3-5% of initial laser power (100mW), 561 nm laser was used 30-40% initial laser power (100mW)). Images were acquired by image streaming for up to 4000 frames at frame rate of 30 frames/s. Active synapses were identified by incubating hippocampal neurons 20 min before imaging with a fluorescently coupled antibody against the luminal domain of Synaptotagmin1 (Synaptic systems Cat.-Nr. 105311CpH for 20min in culture media diluted 1:200 within cultured media), which did allow the identification of active synapses (Kraszewski et al., 1995). In some experiments cells were pre-incubated with BAPTA- or EGTA-AM (20 µM) for 30 minutes.

Localization and trajectory reconnection of mEOS2 signals was performed by the use of a wavelet based algorithm (Izeddin et al., 2012). Single mEos2 molecule fluorescence could be identified by occurrence of fluorescence in the red channel and the defined minimum duration of fluorescence. Trajectories of mEos2-tagged molecules were reconstructed by a simulated annealing algorithm (Racine et al., 2006), taking into account molecule localization and total intensity. It has been described that mEOS2 molecules can show blinking-like behavior ((Annibale et al., 2011), Fig. S3). To avoid false reconnections between trajectories, all sub-trajectories of mEos2 were analyzed as individual trajectories. The dynamic behavior of single molecules was computed from the MSD curves for all trajectories of at least 8 frames. Diffusion coefficients were calculated by linear fit of the first four points of the MSD plots. MSD plots of immobilized molecules (on fixed samples) revealed that under our imaging conditions only $D \geq 0.002$ µm²/s can be considered to be mobile. The calculation of the explored area for synaptic located molecules was performed on trajectories longer than 20 time points in order to fit the MSD according to the procedure described by (Kusumi et al., 1993).

Monte-Carlo simulation

A discrete space-time simulation based on random walk theory was developed using MatLab (Release 2013b – 8.2.0.701). The channel dynamics were modelled on a two-dimensional lattice. The

basic lattice unit size was set to 10 nm corresponding to typical geometry values given in (Nadkarni et al., 2010; Ribrault et al., 2011; Shahrezaei and Delaney, 2004). Ca^{2+} channels were modelled by a central unit of 10 x 10 nm, i.e. one lattice unit, surrounded by 8 boundary units. The dynamical movement of Ca^{2+} channels was simulated as a random walk in 2D, i.e. random moves into four possible directions with equal probability. This movement was limited due to two reasons. First, channels could not extend the movement beyond a given membrane boundary. The 2D membrane size was selected according to the microscopic observations and given values from the literature between 300 x 300 nm and 500 x 500 nm. Second, the channel movement was limited to free membrane spaces, i.e. channels could not overlap with each other. The time step of the simulation was chosen so that the median diffusion coefficient of 0.02 μm^2/s was observed for a freely moving channel. The initial channel positions were randomly selected under the condition that no channel overlap was observed. The channel positions were then tracked over a step period of about 50-100 simulation steps. The mean square deviation of every channel and, based on this, the diffusion coefficient for every channel was calculated from this data. The simulation procedure was repeated 100 times with a new set of random numbers each time to get a statistical average of the diffusion coefficient distribution. Different random number generators of MatLab (*Mersenne, Twister, Congruential*) were applied and no significant influence on the results could be observed.

The obtained channel positions after the movement served as the initial configuration for the second part of our Monte-Carlo simulation, the random walk simulation of Ca^{2+} ions above the membrane. Here every channel location served as the initial inserting location of a Ca^{2+} ion. The Ca^{2+} ion could then move as a random walker in 3D during a simulation time step, i.e. into six different directions. The step time was selected to match the Ca^{2+} diffusion coefficient of about 50 μm^2/s given by (Nadkarni et al., 2010). This movement was only limited by the membrane surface itself, i.e. the Ca^{2+} ions could not move below the membrane surface. We investigated the Ca^{2+} ion concentration in a vicinity of 10 nm above the membrane and used a lattice spacing of 1 nm for the unit size in z-direction. Ca^{2+} ions were released from every channel position according to a 50% probability and moved afterwards according to a random walker. The simulation was carried out until around 300-500 Ca^{2+} ions were released by each channel corresponding to the values given in (Shahrezaei and Delaney, 2004; Stanley, 1993). The random positions of all Ca^{2+} ions were recorded and used to calculate the ion concentration above the membrane. An averaging procedure has been used where all ions in a xyz-box of 10 x 10 x 5nm were summed up and transformed to a molar ion concentration. The levels reached compare well to the numbers of around 100-250 μM (Ribrault et al., 2011). Based on this Ca^{2+} ion concentration a coefficient of variation CV_A was estimated. For this parameter, the average ion concentration value at the height of 5 nm above the membrane was compared to a local value of a coarse-grained lattice where 3 x 3 lattice units, i.e. 30 x 30nm, were taken together for the estimation of the discrete Ca^{2+} ion number in each such box. If the ion numbers are equal to the average everywhere above the membrane, the coefficient of variation is small and close to zero. If there are strong differences between the average value and the local values this parameter is large and closes to one. In order to calculate a corresponding vesicle release probability P_r we randomly placed a number of vesicles from 1-10 at a distance of 5 nm above the membrane and estimated the number of Ca^{2+} ion in the local vicinity at a radius of about 20 nm around each vesicle. If the number of Ca^{2+} ions in the vicinity of the vesicle exceeds a threshold value of eight calcium ions, corresponding to a molar concentration of 250 μM, the release of the vesicle is triggered. The

probability values are estimated based on 100 repeated simulations, the statistical value is given as mean value and standard deviation. Each simulation used a different set of random numbers and the random number generators provided by MatLab (*Mersenne, Twister, Congruential*) were used interchangeably in order to ensure independence of the applied pseudo-random number distributions.

Statistic

The statistical significance of the results was probed by various tests given in the figure legend and main text. We used GraphPad Prism 5.0 software to compare data. Data are represented either as means ± SEM, mean ± SD or medians with interquatril range (IQR) stated in the figure legends, depending on the data distribution. Significance level is marked as follow: $p < 0.05$ *, $p < 0.005$ **, $p < 0.0005$ ***.

References:

Annibale, P., Vanni, S., Scarselli, M., Rothlisberger, U., and Radenovic, A. (2011). Quantitative photo activated localization microscopy: unraveling the effects of photoblinking. PLoS One *6*, e22678.

Frischknecht, R., Fejtova, A., Viesti, M., Stephan, A., and Sonderegger, P. (2008). Activity-induced synaptic capture and exocytosis of the neuronal serine protease neurotrypsin. J Neurosci *28*, 1568-1579.

Izeddin, I., Boulanger, J., Racine, V., Specht, C.G., Kechkar, A., Nair, D., Triller, A., Choquet, D., Dahan, M., and Sibarita, J.B. (2012). Wavelet analysis for single molecule localization microscopy. Opt Express *20*, 2081-2095.

Kusumi, A., Sako, Y., and Yamamoto, M. (1993). Confined lateral diffusion of membrane receptors as studied by single particle tracking (nanovid microscopy). Effects of calcium-induced differentiation in cultured epithelial cells. Biophys J *65*, 2021-2040.

Lin, Y., McDonough, S.I., and Lipscombe, D. (2004). Alternative splicing in the voltage-sensing region of N-Type CaV2.2 channels modulates channel kinetics. J Neurophysiol *92*, 2820-2830.

Nadkarni, S., Bartol, T.M., Sejnowski, T.J., and Levine, H. (2010). Modelling vesicular release at hippocampal synapses. PLoS Comput Biol *6*, e1000983.

Racine, V., Hertzog, A., Jouaneau, J., Salamero, J., Kervrann, C., and Sibarita, J.-B. (2006). Multiple target tracking of 3D fluorescent objects based on simulated annealing. Proceedings of the IEEE International Symposium on Biomedical Imaging *ISBI'2006*, 1020–1023.

Ribrault, C., Sekimoto, K., and Triller, A. (2011). From the stochasticity of molecular processes to the variability of synaptic transmission. Nat Rev Neurosci *12*, 375-387.

Shahrezaei, V., and Delaney, K.R. (2004). Consequences of molecular-level Ca2+ channel and synaptic vesicle colocalization for the Ca2+ microdomain and neurotransmitter exocytosis: a monte carlo study. Biophys J *87*, 2352-2364.

Stanley, E.F. (1993). Single calcium channels and acetylcholine release at a presynaptic nerve terminal. Neuron *11*, 1007-1011.

Szabo, Z., Obermair, G.J., Cooper, C.B., Zamponi, G.W., and Flucher, B.E. (2006). Role of the synprint site in presynaptic targeting of the calcium channel CaV2.2 in hippocampal neurons. Eur J Neurosci *24*, 709-718.

Tsuriel, S., Geva, R., Zamorano, P., Dresbach, T., Boeckers, T., Gundelfinger, E.D., Garner, C.C., and Ziv, N.E. (2006). Local sharing as a predominant determinant of synaptic matrix molecular dynamics. PLoS Biol *4*, e271.

Kraszewski, K., Mundigl, O., Daniell, L., Verderio, C., Matteoli, M., and De Camilli, P. (1995). Synaptic vesicle dynamics in living cultured hippocampal neurons visualized with CY3-conjugated antibodies directed against the lumenal domain of synaptotagmin. J Neurosci *15*, 4328-4342.